nature communications

Article

https://doi.org/10.1038/s41467-024-50688-0

Imaging-guided companion diagnostics in radiotherapy by monitoring APE1 activity with afterglow and MRI imaging

Received: 15 November 2023

Accepted: 18 July 2024

Published online: 28 July 2024

Check for updates

Renye Yue[1,2], Zhe Li[1], Huiyi Liu[1], Youjuan Wang[1], Yuhang Li[3], Rui Yin[1], Baoli Yin[1], Haisheng Qian[2], Heemin Kang[4], Xiaobing Zhang[1] & Guosheng Song[1,5]

Companion diagnostics using biomarkers have gained prominence in guiding radiotherapy. However, biopsy-based techniques fail to account for real-time variations in target response and tumor heterogeneity. Herein, we design an activated afterglow/MRI probe as a companion diagnostics tool for dynamically assessing biomarker apurinic/apyrimidinic endonuclease 1(APE1) during radiotherapy in vivo. We employ ultrabright afterglow nanoparticles and ultrasmall $FeMnO_x$ nanoparticles as dual contrast agents, significantly broadening signal change range and enhancing the sensitivity of APE1 imaging (limit of detection: 0.0092 U/mL in afterglow imaging and 0.16 U/mL in MRI). We devise longitudinally and transversely subtraction-enhanced imaging (L&T-SEI) strategy to markedly enhance MRI contrast and signal-to-noise ratio between tumor and normal tissue of living female mice. The combined afterglow and MRI facilitate both anatomical and functional imaging of APE1 activity. This probe enables correlation of afterglow and MRI signals with APE1 expression, radiation dosage, intratumor ROS, and DNA damage, enabling early prediction of radiotherapy outcomes (as early as 3 h), significantly preceding tumor size reduction (6 days). By monitoring APE1 levels, this probe allows for early and sensitive detection of liver organ injury, outperforming histopathological analysis. Furthermore, MRI evaluates APE1 expression in radiation-induced abscopal effects provides insights into underlying mechanisms, and supports the development of treatment protocols.

Radiation therapy is a widely used treatment modality for cancer patients, with the objection of targeting and eliminating tumor tissue through the induction of DNA damage via ionizing radiation (e.g., X-ray)[1]. However, the heterogeneity of tumors and individual variations necessitate a personalized approach to radiotherapy for improving treatment effectiveness and minimizing adverse effects[2,3]. Companion diagnostics, an emerging technology, aims to develop suitable diagnostic and treatment strategies based on individual patients' therapeutic responses to specific biomarkers[4,5]. Currently, most FDA-approved biomarkers for companion diagnostics are assessed through in vitro or ex vivo biopsy-based analysis, which fails to account for tumor heterogeneity in different individuals and real-time changes in target response in living systems[5–7]. Imaging-guided companion diagnostics, such as MRI, PET, SPECT, or photoacoustic imaging, offer real-

[1]State Key Laboratory of Chemo/Biosensing and Chemometrics, College of Chemistry and Chemical Engineering, Hunan University, Changsha, PR China. [2]School of Biomedical Engineering, Research and Engineering Center of Biomedical Materials, Anhui Medical University, Hefei, PR China. [3]Department of Hepatobiliary Surgery/Central Laboratory, Hunan Provincial People's Hospital (The First Affiliated Hospital of Hunan Normal University), Changsha, PR China. [4]Department of Materials Science and Engineering and College of Medicine, Korea University, Seoul, South Korea. [5]Shenzhen Research Institute, Hunan University, Shenzhen, China. e-mail: songgs@hnu.edu.cn

time, non-invasive, and dynamic insights into biomarker status in vivo, surpassing the capabilities of in vitro or ex vivo analysis techniques[8–11]. Combining imaging-based companion diagnostics with radiotherapy has the potential to facilitate personalized dose prescriptions based on real-time biomarker activity, addressing the challenges posed by tumor heterogeneity and individual variations[12]. However, there are rare reports using molecular imaging technology for companion diagnostics in external beam radiation therapy (Supplementary Table 1).

The selection of biomarkers is crucial for imaging-guided companion diagnostics in radiotherapy[6]. While several biomarkers have been introduced for predicting tumor response and tissue toxicity under radiotherapy, utilizing a single biomarker for analyzing DNA damage or ROS level alone is insufficient for a comprehensive evaluation or prediction of radio-sensitivity, radio-resistance, or radio-induced toxicity[3,13–15]. A key protein called apurinic/apyrimidinic endonuclease 1 (APE1) has been identified as playing a pivotal role in regulating cell response to oxidative stress and repairing damaged DNA during radiotherapy[16,17], making it a potential biomarker for monitoring and predicting therapeutic outcomes and radiation-associated toxicity[18]. Currently, several methods exist for detecting APE1, including enzyme-linked immunosorbent assay, electrophoresis radioactivity, electrochemiluminescence methods, liquid chromatography-mass spectrometry, and Western Blotting, mostly in cells or ex vivo[19,20]. Recently, spatially selective monitoring of APE1 level in mitochondria in cancer cells through fluorescence imaging has been employed to evaluate the outcome of photodynamic therapy[21–23]. Several fluorescence probes labeled with Cyanine have also been used for real-time imaging of APE1 in cancer cells (Supplementary Table 2), however, those fluorescence probes may suffer from autofluorescence interference and inadequate imaging depth[24–26].

Afterglow luminescence, also known as long-persistent luminescence, offers delayed luminescent signals after cessation of light irradiation with ultrahigh signal-to-noise ratio compared to fluorescence imaging[27–29], eliminating the need for real-time light excitation and reducing autofluorescence of biological tissues[10,30–32]. However, current afterglow imaging techniques face challenges such as low afterglow intensity, high laser excitation requirements, rapid signal attenuation, and toxicity, limiting their application for imaging APE1 activity, resulting in no report about afterglow imaging for APE1. Magnetic resonance imaging (MRI), a versatile clinical diagnostic technology, offers non-invasive and high-resolution imaging, as well as precise structural information for intratumor biomarkers[33,34]. However, there have been no reports on MRI imaging of APE1 until now, due to the intrinsic low sensitivity of MRI technology[35,36]. Therefore, combining the advantages of afterglow luminescence and MRI imaging can provide molecular information on APE1 level and offer both anatomical and functional imaging for APE1 activity based on MRI and afterglow.

In this study, we develop a core-satellite structure, with the core consisting of an afterglow nanoparticle (TA NPs) as a luminescence donor and the satellites comprising quencher molecule-labeled $FeMnO_x$ nanoparticles serving as an afterglow acceptor and MRI contrast agents (Fig. 1). This design strategically positioned the APE1-cleaved sites outside of the probe, minimizing steric hindrance for enzyme cleavage and improving the efficiency of APE1 cleavage. The ultrabright afterglow nanoparticle has developed for imaging APE1 activity in deep-seated tissues of living animals. Additionally, in a buffered solution environment, our system significantly extends the detectable range of APE1 concentration to 0–4 U/mL and improves the detection sensitivity with a limit of detection of 0.0092 U/mL. Ultrasmall manganese-doped iron oxide nanoparticles ($FeMnO_x$) as dual contrast agents in both T_1 and T_2 MRI models[37,38], significantly amplifies the signal dynamic ranges, detection range, and detection sensitivity (limit of detection: 0.16 U/mL) for APE1. This enabled real-time, whole-body imaging for APE1 activity in living mice with high sensitivity, based on MRI technology. Additionally, we develop a longitudinally and transversely subtraction-enhanced imaging (L&T-SEI) strategy to further enhance MRI contrast of APE1-probe for tumors. Specifically, the APE1-responsive afterglow/MRI probe is performed as a companion diagnostics tool for early monitoring of tumor response and toxicity during radiotherapy in living female mice. The probe specifically targets the tumor, enabling real-time imaging of APE1 activity through afterglow luminescence and MRI imaging. Notably, it demonstrates correlations between afterglow and MRI signals with radiation dose-dependent APE1 expression, intratumor ROS yield, intratumor DNA damage, and therapeutic outcome. This valuable companion diagnostics tool can monitor APE1 levels in tumors, offering early prediction of radiotherapeutic outcomes. Exceptionally, the probe rapidly detects radiation dose-induced APE1 expression as early as 3 h, much earlier than the shrinkage in tumor size (6 days). Additionally, the APE1-responsive afterglow/MRI probe is utilized for evaluating radiation-induced liver organ injury. It provides a more sensitive, earlier, and dynamic evaluation of liver organ injury, reducing detection time windows. Furthermore, MRI imaging is used to evaluate the APE1 level in radiation-induced abscopal effect, providing insights into the underlying mechanisms and optimizing treatment protocols.

Results and discussion

Programmed self-assembly for APE1-activated core-satellite nanoprobe

In order to achieve high-sensitivity afterglow imaging, we synthesized trianthracene derivatives (TA) based on the previous report (Supplementary Fig. 1)[39]. The successful synthesis of TA molecules was confirmed through MALDI-TOF mass spectroscopy (Supplementary Figs. 2–8). By employing an electron transfer strategy, we greatly improved afterglow luminescence intensity. Subsequently, we synthesized afterglow nanoparticles (TA NPs) through one-step nanoprecipitation using electron-rich trianthracene molecules, a semiconducting polymer (PFODBT), polymethacrylates (PSMA), and a polyethylene-polypropylene glycol polymer (F127) (Fig. 2a). Notably, the addition of PFODBT enhanced the structural rigidity of nanoparticles. PSMA was employed to introduce the carboxyl group on the surface of TA NPs for subsequent modification. The as-prepared TA NPs had a mean diameter of 34 ± 8 nm, as determined by transmission electron microscopy (TEM) images (Fig. 2b). The average hydrodynamic size of TA NPs in water was measured to be 38 ± 3.9 nm with zeta potential of −18 ± 1.8 mV (Supplementary Fig. 9). Additionally, TA NPs exhibited a maximal absorption wavelength of 595 nm and a fluorescent emission wavelength of 630 nm, as evidenced by the spectra (Supplementary Fig. 10), which supported the quantification of TA NP concentrations using the relative standard curve of the absorption of TA molecules at 595 nm (Supplementary Fig. 11).

To characterize the afterglow luminescence of TA NPs, we initially optimized the irradiation parameters for exciting the afterglow signal. White light irradiation time was varied from 0 to 60 s (10 mW/cm^2, 0–60 s) while keeping the acquisition time fixed at 60 s to promote afterglow signal generation. The results showed that an irradiation time of 10 s was optimal for exciting the strongest afterglow luminescence (Supplementary Fig. 12). Furthermore, to determine a suitable acquisition time, we varied the acquisition time from 1 to 100 s while maintaining a fixed irradiation time of 10 s (10 mW/cm^2) to collect the afterglow signal. It was observed that a more stable and stronger afterglow signal was obtained at an acquisition time of 60 s (Supplementary Fig. 13). Besides, under increasing power density, TA NPs exhibited a corresponding enhancement in the afterglow signal (Supplementary Fig. 14). Moreover, to determine the half-life period of the afterglow luminescence signal, TA NPs were irradiated with a radiation time of 10 s, and the afterglow signal was collected with an

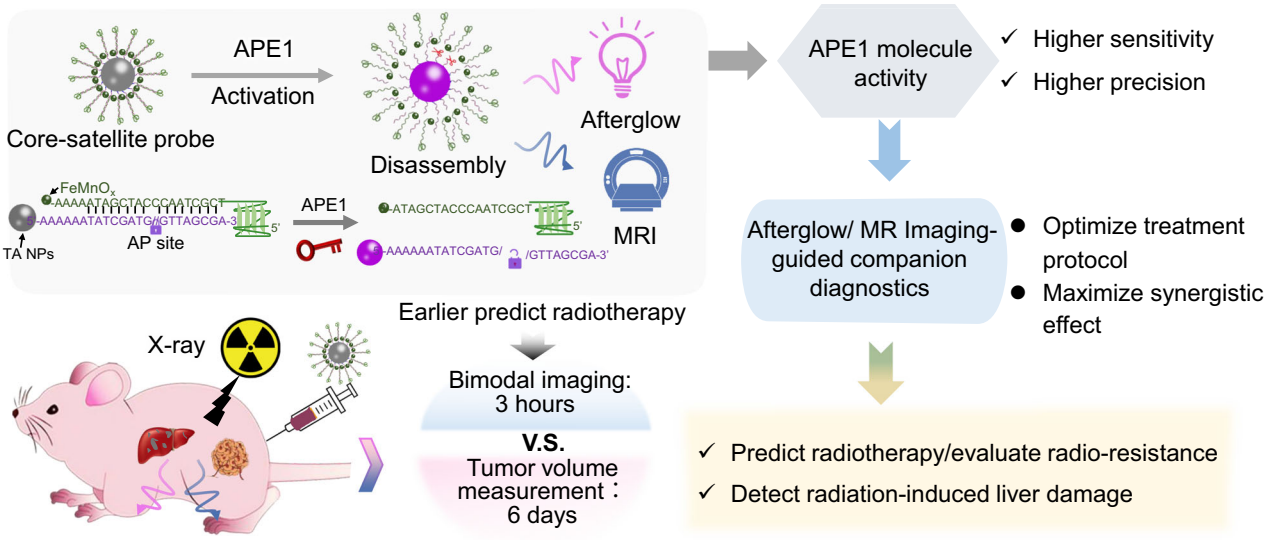

Fig. 1 | APE1-responsive afterglow/MRI probe for monitoring of tumor response as a companion diagnostics tool during radiotherapy.

acquisition time of 60 s. Continuous acquisition of afterglow images revealed that the long-lasting afterglow luminescence of TA NPs persisted for over 60 min after cessation of light, with a prolonged half-life of ~15 min (Fig. 2c, d and Supplementary Fig. 15). This half-life was even longer than that of common afterglow materials, such as MEHPPV-based nanoparticles, which have a half-life of about 6 min[10,32]. Finally, we recharged TA NPs through 10 cycles of light irradiation and observed that the maximum afterglow intensity of TA NPs did not exhibit any significant decay (Fig. 2e, f and Supplementary Fig. 16), ensuring accurate quantification of afterglow signals during prolonged and repeated molecular imaging (Supplementary Table 3). Notably, compared to common organic afterglow molecules (such as MEHPPV or its analog), afterglow NPs exhibited an ultra-strong afterglow luminescence that was significantly higher than that of MEHPPV-based nanoparticles (Fig. 2g, h).

Next, we modified TA NPs with amino-labeled DNA1 through a cross-linking reaction (Fig. 2a). The successful preparation of TA NPs-DNA1 was confirmed by the enhanced absorption intensity of DNA1 at 260 nm compared to free TA NPs-COOH (Supplementary Fig. 17). Additionally, the dynamic light scattering (DLS) analysis revealed an increase in the diameter to 48.4 nm ± 4.0 nm (Supplementary Fig. 18). The modification ratio of DNA1/TA NPs was determined to be 250 mmol DNA1/2 g TA NPs based on the absorbance of excess DNA1 at 260 nm (Supplementary Fig. 19).

For the synthesis of magnetic nanoparticles as MRI contrast agents, ultrasmall $FeMnO_x$ was prepared through thermal decomposition using iron-eructate and manganese-oleate[37]. The TEM images revealed that the as-synthesized $FeMnO_x$ had a mean diameter of 3.4 ± 0.9 nm (Fig. 2i), corresponding to a DLS size of 3.2 ± 0.2 nm in $CHCl_3$ (Supplementary Fig. 20). In addition, more characterizations such as X-ray diffraction (*XRD*), X-ray photoelectron spectroscopy (*XPS*), energy dispersive X-ray analysis (*EDX*), further confirmed the successful preparation of $FeMnO_x$ nanoparticles. Subsequently, $FeMnO_x$ was modified with phosphorylated/azide-polyethylene glycol (p-PEG-N_3) and 2-bromo-2-methylpropanoic acid (BMPA) through a ligand exchange process to yield $FeMnO_x$-N_3, which was further modified with amino-modified BHQ_3 quencher molecules (H_2N-BHQ_3) to form $FeMnO_x$@BHQ_3-N_3 (Fig. 2a). The successful preparation resulted in the transformation of hydrophobic $FeMnO_x$ (yellow color) into hydrophilic $FeMnO_x$@BHQ-N_3 (green color) (Supplementary Fig. 21). $FeMnO_x$@BHQ_3-N_3 exhibited noticeable absorbance of BHQ_3 at the wavelength of 600 nm, with an average hydrodynamic diameter of 9.6 ± 0.8 nm and a potential of −14 ± 0.2 mV. Fourier-transformed infrared (FTIR) spectra indicated the conjugation of BHQ_3 on $FeMnO_x$. We determined the MRI contrast ability of $FeMnO_x$@BHQ-N_3 using a 7T-MRI scanner. From MRI images (Fig. 2j, k), monodispersed $FeMnO_x$@BHQ-N_3 displayed increased brightness (positive contrast) in T_1 MRI images, while demonstrating darkness (negative contrast) in T_2 MRI images as the $FeMnO_x$ concentration increased, suggesting contrast ability in T_1 MRI and T_2 MRI.

Subsequently, $FeMnO_x$@BHQ_3-N_3 was conjugated with alkyne-labeled DNA2 (alkyne-DNA2) through the click reaction, resulting in the formation of DNA2-functionalized $FeMnO_x$@BHQ_3-N_3 ($FeMnO_x$-DNA2) (Fig. 2a). The preparation of $FeMnO_x$-DNA2 was confirmed by an increase in the DLS size to 12.9 ± 1.1 nm and a decrease in zeta potential to −16.1 ± 1.4 mV (Supplementary Fig. 22). Based on the hybridization of DNA1 and DNA2, we assembled TA NPs-DNA1 with $FeMnO_x$-DNA2 to form the core-satellite assembly of TA NPs and $FeMnO_x$, named APE1-probe (Fig. 2a and Supplementary Fig. 23). The preparation of APE1-probe was verified through TEM images, which revealed a core-satellite structure where afterglow NPs served as the core and multiple $FeMnO_x$ acted as satellites attached closely to the surface of TA NPs (Fig. 2l). The DLS analysis determined an average diameter of 83.0 ± 7.2 nm with a potential of −37 ± 2.6 mV, and showed excellent colloidal stability in different buffer over the observed time period (Supplementary Fig. 24).

Due to the spectral overlap between the absorption of $FeMnO_x$@BHQ_3 and the afterglow luminescence of TA NPs (Fig. 2m), the close attachment of multiple $FeMnO_x$ onto the surface of TA NPs would quench TA NPs' afterglow signal by adjacent BHQ_3 molecules through afterglow resonance energy transfer (ARET) (Fig. 2n). To confirm this, we compared the afterglow signal intensity of TA NPs-DNA1 before and after assembling with $FeMnO_x$-DNA2. As anticipated, the afterglow luminescence of TA NPs was significantly quenched to ~95.0 ± 3.0% by BHQ_3 molecules within $FeMnO_x$-DNA2 (Fig. 2o), suggesting $FeMnO_x$-DNA2. This reduction of the afterglow signal before the response was advantageous to decreasing the initial afterglow signal, enhancing the signal-to-noise ratio, and expanding the dynamic range. Additionally, we optimized the assembly ratio of TA NPs-DNA1 and $FeMnO_x$-DNA2 (Fig. 2p and Supplementary Fig. 25). We observed that as the assembly ratio between $FeMnO_x$-DNA2 and TA NPs-DNA1 increased, the afterglow signal decreased. According to the afterglow signal, we chose a suitable ratio of 25 μg $FeMnO_x$-DNA2/2 μg TA NPs-DNA1 for the preparation of APE1-probe in subsequent experiments.

https://doi.org/10.1038/s41467-024-50688-0

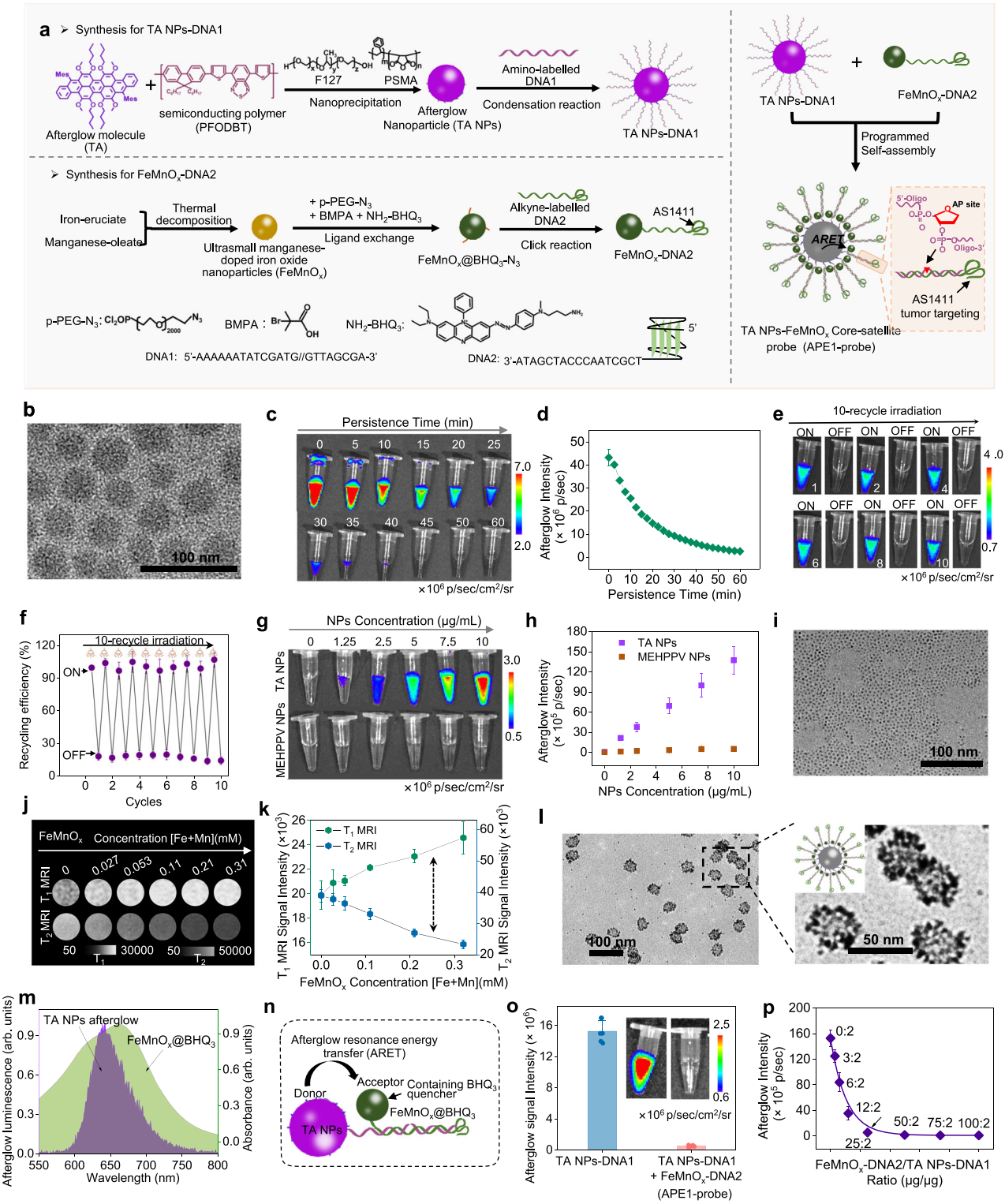

Fig. 2 | Preparation and characterization of TA NPs-FeMnO$_x$ assembly (APE1-probe). **a** Schematic illustration for afterglow luminescent mechanisms of TA NPs and preparation of APE1-probe. **b** Representative TEM images of TA NPs ($n = 3$ independent samples). **c**, **d** Afterglow images and signal attenuation of TA NPs after irradiation (30 μg/mL, $n = 3$ independent samples). **e**, **f** Afterglow images and signal intensity of TA PNs under 10-recycle recharge (30 μg/mL, $n = 6$ independent samples). **g**, **h** Afterglow images and signal intensity of TA NPs nanoparticle and MEHPPV-based nanoparticle ($n = 3$ independent samples). **i** Representative TEM images of FeMnO$_x$ ($n = 3$ independent samples). **j**, **k** MRI images and signal intensity of various concentrations of FeMnO$_x$@BHQ$_3$-N$_3$ ($n = 3$ independent samples). **l** Representative TEM images of TA NPs-FeMnO$_x$ assembly (APE1-probe) ($n = 3$ independent samples). **m** Overlap of TA NPs-DNA1's afterglow luminescence spectrum and BHQ$_3$'s absorption spectrum. **n** Schematic illustration for the afterglow resonance energy transfer (ARET) between TA NPs donor and BHQ$_3$ quencher. **o** Afterglow images and signal intensity of TA NPs-DNA1(10 μg/mL, $n = 6$ independent samples) before and after assembling with FeMnO$_x$-DNA2. **p** Afterglow signal intensity of TA NPs-DNA1 (10 μg/mL, $n = 6$ independent samples) assembling with various ratio of FeMnO$_x$-DNA2. All afterglow imaging were obtained with white light irradiation (10 mW/cm^2) time of 10 s and acquisition time of 60 s. Data are presented as means ± SD. Source data are provided as a Source Data file.

https://doi.org/10.1038/s41467-024-50688-0

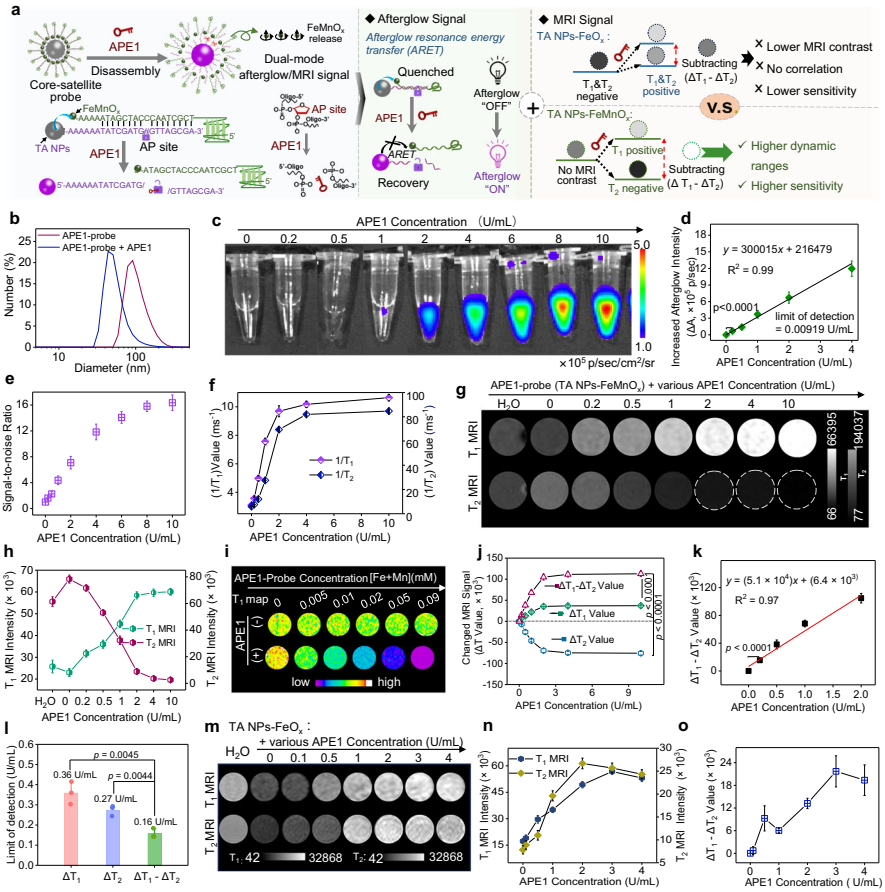

Fig. 3 | APE1-activated afterglow and MRI in APE1-probe solution. a Scheme illustration for APE1-activated TA NPs-FeMnO$_x$ assembly (APE1-probe) for afterglow and MRI contrast comparison between TA NPs-Fe_3O_4 and TA NPs-FeMnO$_x$ (APE1-probe). **b** Hydrodynamic size distribution of APE1-probe before and after incubation with APE1 (10 U/mL). **c**–**e** Afterglow imaging of APE1-probe after incubating with various concentrations of APE1 (0–10 U/mL) (containing 5 μg/mL TA NPs, $n = 6$ independent samples). **c** Afterglow images. **d** A near-liner curve between the afterglow signal and APE1 concentration. **e** Signal-to-noise ratio of afterglow signal. **f**–**l** Relaxation time and MRI measurement of APE1-probe (containing 5 μg/mL TA NPs, $n = 3$ independent samples) treated with various concentrations of APE1. **f** $1/T_1$ and $1/T_2$ values. **g** T_1 MRI and T_2 MRI images. **h** Quantified T_1 and T_2 MRI signal intensity from (**g**). **i** Relaxation time mapping images of different concentrations of APE1-probe before and after APE1 (10 U/mL) incubation. **j** MRI signal range (ΔT_1, ΔT_2, and ΔT_1–ΔT_2 value) of APE1-probe treated with various concentrations of APE1. **k** Correlated curve between ΔT_1–ΔT_2 value and APE1 concentration. **l** Corresponding limit of detection under MRI signal ranges from (**j**). **m**–**o** MRI images and quantification of TA NPs-FeO$_x$ treated with various concentration s of APE1(0–4 U/mL) (containing 5 μg/mL TA NPs, $n = 3$ independent samples). **m** T_1 MRI and T_2 MRI images. **n** Quantified T_1 and T_2 MRI signals from (**m**). **o** ΔT_1–ΔT_2 value calculated from (**n**). All afterglow imaging were obtained with white light irradiation (10 mW/cm^2) time of 10 s and acquisition time of 60 s. Data are presented as means ± SD. Statistical significance was determined using two-tailed Student's *t*-test for pairwise comparisons, and one-way ANOVA analysis of variance for multiple groups. *p* values > 0.05 were considered non-significant, while *p* values < 0.05 were considered statistically significant. Source data are provided as a Source Data file.

Core-satellite probe for afterglow and MRI imaging of APE1 activity with larger dynamic range and higher sensitivity

In the design of APE1-cleavable apurinic/apyrimidinic (AP) sites within the DNA sequence, the APE1-cleaved AP sites were positioned outside of the core-satellite structure in the APE1-probe. We hypothesize that this configuration would reduce steric hindrance at the catalytic sites, thus improving the efficiency of APE1-mediated cleavage, as depicted in Fig. 3a. Consequently, when the double-strands of the DNA1-DNA2 region outside the core-satellite structure encounters the APE1 enzyme, the AP site in DNA1 is promptly cleaved by APE1. This cleavage results in the release of FeMnOx@BHQ_3, which facilitates the rapid recovery of the afterglow signal due to the disruption of the ARET effect between TA NPs and FeMnOx@BHQ_3. Furthermore, the liberation of FeMnO$_x$ from APE1-probe results in its dispersion to release free FeMnO$_x$ nanoparticles, contributing to an enhanced positive contrast in T_1-weighted MRI (manifesting as increased brightness) and an augmented negative contrast in T_2-weighted MRI (resulting in greater darkness).

We incubated the APE1-probe with APE1 enzyme (10 U/mL) and measured the change in their hydration diameter. As illustrated in Fig. 3b, incubation with APE1 caused the average DLS size of APE1-probe to decrease to 49.7 ± 4.1 nm from the original size of APE1-probe (83.0 ± 7.2 nm), confirming that APE1 could trigger the disassembly of APE1-probe by cleaving the AP sites. To further investigate the APE1-dependent afterglow signal recovery, we incubated APE1-probe with varying concentrations of APE1, ranging from 0 to 10 U/mL. After 4 h of incubation, we detected the afterglow signals using an IVIS Lumina XR imaging system under a bioluminescence model, following a 10-s light irradiation. As shown in Fig. 3c and Supplementary Figs. 26 and 27, the afterglow luminescence gradually increased with increasing APE1 concentration, suggesting that APE1 can progressively activate APE1-probe for afterglow signal recovery by cleaving the AP sites and disrupting the ARET effect between TA NPs and FeMnO$_x$@BHQ_3. The afterglow signal recovery was calculated to be 28.0 ± 2.0% in APE1 (4 U/mL) (Supplementary Fig. 28).

Notably, due to the ultrahigh afterglow luminescence of TA NPs, the range of recovered afterglow signal could reach ~10^6 when the APE1 concentration increased from 0 to 10 U/mL (Supplementary Fig. 27). This extensive dynamic range of afterglow signal recovery facilitated

the detection of APE1 over a wide range, without the risk of signal saturation. Consequently, it enabled accurate measurement of APE1 concentration in biological conditions. Additionally, a nearly linear relationship was observed between the increased afterglow signal and APE1 concentration within the range of 0 to 4 U/mL. The limit of detection for the APE1 enzyme was calculated to be 0.0092 U/mL using the formula (3σ/k) (Fig. 3d). This value was significantly lower than that of most fluorescence probes used for APE1 detection (Supplementary table 2). Importantly, the signal-to-noise ratio exhibited an increasing trend as the afterglow signal recovered (Fig. 3e). Taken together, these results demonstrated that the APE1-probe can detect APE1 through afterglow signal recovery, offering a wider signal range (~10^6), a broader detection range for APE1 (0–10 U/mL), and enhanced detection sensitivity (limit of detection: 0.0092 U/mL).

To improve the sensitivity of MRI in detecting APE1, we opted for ultrasmall $FeMnO_x$ as the MRI contrast agent. $FeMnO_x$ demonstrated dual-contrast ability in both T_1 and T_2 MRI models[37,38] (Fig. 2j). Specifically, when a core-satellite probe responsive to APE1 was employed, $FeMnO_x$ nanoparticles detached from the core of the probe, leading to the manifestation of dual-contrast ability in both T_1 and T_2 MRI models as the APE1 concentration increased (Fig. 3a). Using a Bruker Minispec analyzer (60 MHz) and a 7 T MRI scanner, we conducted experiments to observe the MRI signal change when APE1-probe responded to APE1. The relaxation time results indicated that as the APE1 concentration increased from 0 to 10 U/mL, both T_1 and T_2 relaxation times of APE1-probe gradually decreased (Supplementary Fig. 29). This resulted in an increase of $1/T_1$ from 3.1 s^{-1} to 10.6 s^{-1} and an increase of $1/T_2$ from 5.9 m^{-1} to 84.8 s^{-1} (Fig. 3f).

To further investigate the MRI contrast enhancement, we acquired MRI images of APE1-probe treated with various concentrations of APE1. Due to the application of $FeMnO_x$, the initial APE1-probe (0 U/mL of APE1) exhibited no discernible MRI contrast, which facilitated to reduce of the background noise of the APE1-probe itself in normal tissues. In contrast, following incubation with APE1, the T_1 MRI images displayed positive contrast enhancement (increased brightness) and an elevation in T_1 MRI signal intensity as the APE1 concentration increased from 0 to 10 U/mL, as illustrated in Fig. 3g, h. Conversely, the T_2 MRI images gradually darkened, indicating negative contrast enhancement, and the T_2 MRI signal intensity decreased. Furthermore, we employed a 7 T MRI scanner to measure the change of relaxation time as APE1-probe responded to APE1, using T_1 or T_2 mapping sequences. The color-coded mapping images demonstrated that after APE1 treatment, both values of T_1 and T_2 relaxation times decreased for various concentrations of the probe, compared to those in the absence of APE1 (Fig. 3i and Supplementary Fig. 30). Besides, APE1-probe showed high selectivity toward APE1 in solution test (Supplementary Fig. 31).

Given the inverse change in T_1 and T_2 MRI signal intensities, subtracting the T_1 MRI signal intensity from the T_2 MRI signal intensity could significantly enhance the dynamic range of MRI signal change[40,41], thereby improving the sensitivity and detection range of APE1. Thereby, we calculated the increased T_1 MRI signal (ΔT_1 value) and decreased T_2 MRI signal (ΔT_2 value) as APE1 concentration increased from 0 to 10 U/mL. Consequently, the ΔT_1–ΔT_2 values were calculated by subtracting the MRI signal intensity between ΔT_1 value and ΔT_2 value. As expected, the ΔT_1–ΔT_2 values of APE1-probe were significantly amplified to ~10^5, compared with a single T_1 MRI or T_2 MRI signal of ~10^4, as demonstrated in Fig. 3j. This amplified response signal greatly enhanced the sensitivity of MRI. Notably, a close linear relationship between ΔT_1–ΔT_2 value and APE1 concentration was observed within the range of 0 to 2 U/mL, as depicted in Fig. 2k. Accordingly, the limit of detection for APE1 was calculated to be 0.16 U/mL. In comparison, using the single ΔT_1 value or ΔT_2 value to correlate with APE1 resulted in a limit of detection values of 0.36 U/mL and 0.27 U/mL, respectively (Fig. 3l). Therefore, subtracting the T_1 MRI signal from the T_2 MRI signal can significantly amplify the MRI dynamic range from 10^4 to 10^5, expand the APE1 detection range (0–10 U/mL), and increase the detection sensitivity (limit of detection: 0.16 U/mL), compared to using a single T_1 MRI signal or single T_2 MRI signal for APE1 quantification.

Ultrasmall iron oxide nanoparticles (FeO_x) have been reported as a positive contrast agent in T_1 MRI imaging studies[42,43]. We also compared the MRI contrast effect of FeO_x, commonly used as a T_1 contrast agent in MRI imaging studies. In this study, we utilized ultrasmall FeO_x nanoparticles (3.9 ± 0.5 nm) as a control group to demonstrate the superior performance of $FeMnO_x$ in our designed system (Supplementary Fig. 32). We compared the MRI contrast effect of FeO_x to that of $FeMnO_x$ nanoparticles. As shown in Supplementary Fig. 33, FeO_x exhibited an increasing brightness in both T_1 and T_2 MRI images as the FeO_x concentration increased. We further explored the use of FeO_x as an MRI contrast agent in the synthesis of TA NPs-FeO_x, achieved by assembling FeO_x-DNA2 with TA NPs-DNA1, as illustrated in Supplementary Fig. 34. Initially, TA NPs-FeO_x exhibited negative contrast in both T_1 and T_2 MRI models until activated by APE1. Following activation, TA NPs-FeO_x demonstrated positive imaging capability in both T_1 and T_2 MRI models (Fig. 3m). However, it is important to note that the MRI signal intensity increased simultaneously with increasing APE1 concentration (Fig. 3n), thereby subtracting the T_1 MRI signal intensity from the T_2 MRI signal intensity (ΔT_1–ΔT_2) would not expand the dynamic range of MRI, compared with that of TA NP-$FeMnO_x$ (Fig. 3g). Furthermore, the ΔT_1–ΔT_2 values of TA NPs-FeO_x were not correlated with the concentration of APE1(Fig. 3o), suggesting that the ΔT_1–ΔT_2 values of TA NPs-FeO_x cannot be used to quantify the concentration of APE1. These results demonstrated the superiority of using $FeMnO_x$ in constructing the APE1-probe, facilitating a higher MRI contrast, higher dynamic ranges, and higher sensitivity for APE1 detection.

APE1-activated afterglow/MRI imaging for monitoring radiation dose-dependent APE1 expression in cancer cells

During radiotherapy, X-rays are utilized to induce DNA damage and the generation of reactive oxide species, aiming to eliminate tumor cells[44]. The extent of DNA damage and oxidative stress is directly influenced by the administered radiation dose[44]. Interestingly, when cancer cells are exposed to increasing doses of X-ray radiation, they upregulate the expression of APE1[45,46]. APE1 is involved in the base excision repair process for damaged DNA repairment or activates transcription factors to balance the intracellular redox environment and reduce oxidative stress[17,47]. Consequently, the upregulated APE1 promotes tumor growth, increases tumor burden, and inhibits the radiosensitivity of tumors[48]. Therefore, APE1 may serve as a potential companion diagnostics biomarker for monitoring and predicting therapeutic outcomes, as well as radiation-associated toxicity during radiotherapy. To monitor the radiation dose-dependent upregulation of APE1 expression, we proposed the utilization of dual-mode imaging by combining afterglow and MRI.

Firstly, we prepared an APE1-irresponsive probe (APE1-ir-probe) consisting of TA NPs-DNA3 and $FeMnO_x$-DNA2 to demonstrate that the change in afterglow and MRI was indeed induced by APE1 cleaving the AP sites and the disassembly of $FeMnO_x$ and TA NPs (Fig. 4a). The DNA3 sequence was similar to DNA1 but did not contain AP sites cleaved by APE1, as shown in Supplementary Fig. 23. The DLS size and Zeta potential data confirmed the preparation of APE1-ir-probe (Supplementary Fig. 35). We incubated APE1-ir-probe with APE1 (10 U/mL) or not, and measured the changes in the afterglow signal and MRI images. Figure 4b shows that no significant enhancement of the afterglow signal was observed before or after APE1-ir-probe incubating with APE1. Moreover, both T_1 MRI and T_2 MRI images exhibited no apparent change in the MRI signal, as depicted in Fig. 4c, d. These results indicated no disassembly of $FeMnO_x$ from TA NPs in APE1-ir-probe treated with APE1. Thus, these findings confirmed that the response of APE1-probe in afterglow and MRI was indeed caused by the

https://doi.org/10.1038/s41467-024-50688-0

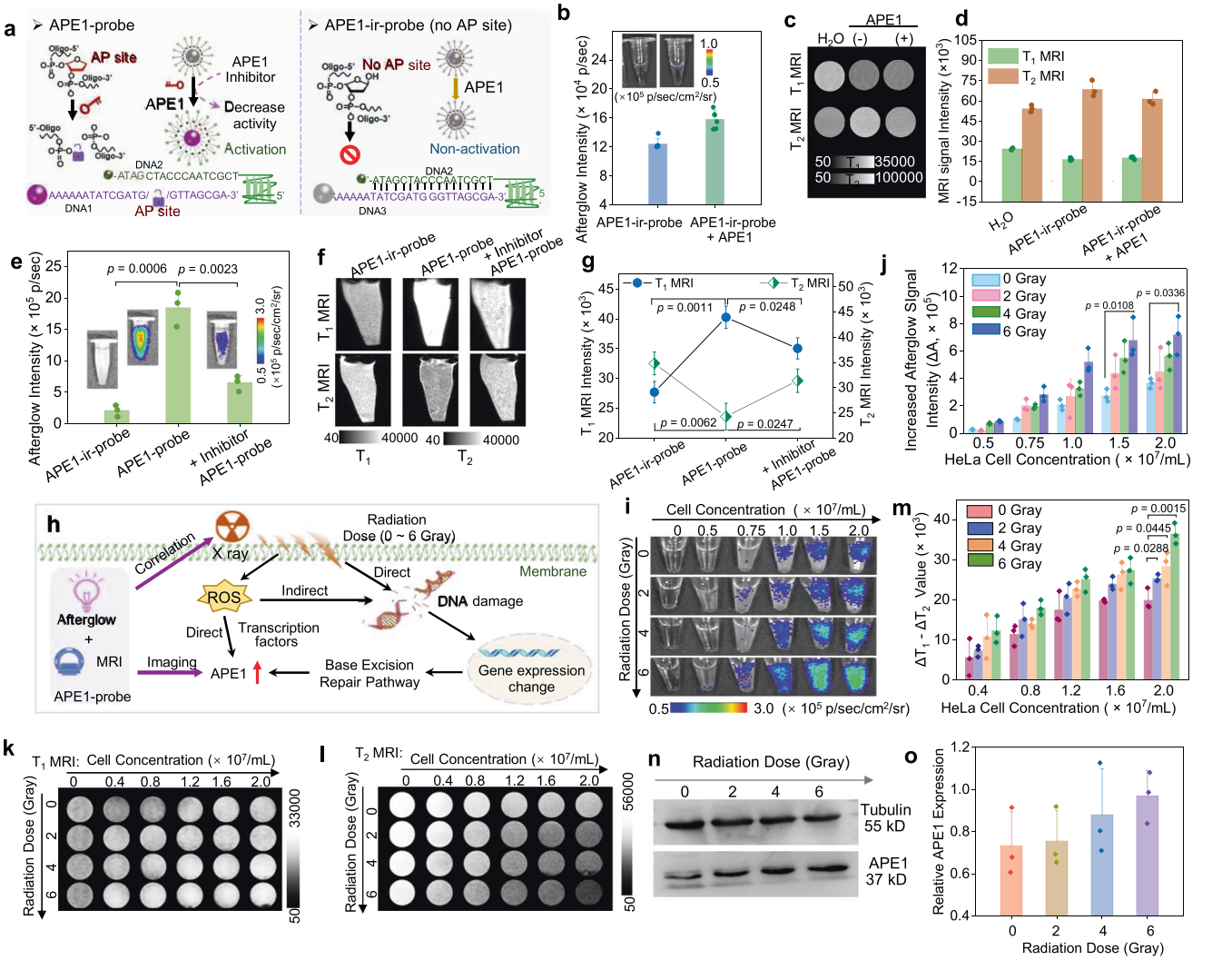

Fig. 4 | APE1-activated afterglow/MRI imaging for monitoring radiation dose-dependent APE1 expression in cancer cells. a Scheme illustration and DNA sequences of the irresponsive probe (APE1-ir-probe, no contain AP sites) and responsive probe (APE1-probe, containing AP sites). **b**, **c** APE1-ir-probe (containing 5 μg/mL TA NPs) incubated with APE1 (10 U/mL) or not ($n = 6$ independent samples). **b** Afterglow images and quantified signal intensity. **c** T_1 and T_2 MRI images ($n = 3$ independent samples). **d** Quantified MRI signal intensity from (**c**). **e**–**g** The HeLa cells incubated with APE1-ir-probe, APE1-probe, and APE1 inhibitor/APE1-probe respectively, for afterglow/ MRI imaging (4×10^7 cells/mL, $n = 3$ independent biological samples) after DPBS washing. **e** Afterglow images and signal intensity. **f** T_1 and T_2 MRI images. **g** Quantified T_1 and T_2 MRI signal intensity. **h** Scheme illustration of dual-mode afterglow/MRI for monitoring radiation dose-dependent APE1 activity. **i**–**m** A various number of HeLa cells treated with various radiation doses (0, 2, 4, and 6 Gray) and then incubated with APE1-probe, for afterglow/ MRI imaging ($n = 3$ independent biological samples) after DPBS washing. **i** Afterglow images. **j** Afterglow signal intensity. **k** T_1 MRI images. **l** T_2 MRI images. m Subtracted MRI signal intensity (ΔT_1–ΔT_2 value). **n**, **o** Western bolting determination and quantified APE1 level of the HeLa cells at post-treatment of 2 h under various radiation doses ($n = 3$ independent biological samples). All cell afterglow imaging was obtained with white light irradiation (10 mW/cm²) time of 10 s and acquisition time of 60 s. Data are presented as means ± SD. Statistical significance was determined using a two-tailed Student's *t*-test for pairwise comparisons, and a one-way ANOVA analysis of variance for multiple groups. *p* values > 0.05 were considered non-significant, while *p* values < 0.05 were considered statistically significant. Source data are provided as a Source Data file.

specific cleavage of AP sites outside of APE1-probe by APE1, leading to the disassembly of $FeMnO_x$@BHQ_3 from TA NPs.

Next, we investigated the specificity of APE1-probe for imaging intracellular APE1. Human cervical cancer cells (HeLa cells) were chosen as the target cancer cells. Three groups were established: (1) HeLa cells incubated with an APE1-irresponsive probe (APE1-ir-probe), (2) HeLa cells incubated with an APE1-responsive probe (APE1-probe), and (3) HeLa cells incubated with an APE1 inhibitor (CRT0044876) to inhibit APE1 activity and APE1-probe[48,49]. Subsequently, all cell suspensions from the three groups were subjected to afterglow/MRI imaging. After analyzing the afterglow images and signal intensity (Fig. 4e), it became evident that cells incubated with APE1-ir-probe did not exhibit significant afterglow signal recovery. Conversely, cells treated with APE1-probe displayed pronounced afterglow signals, confirming the ability of APE1-probe to detect intracellular APE1 levels. Additionally, the cells treated with APE1 inhibitor+ APE1-probe revealed a decrease in afterglow signal associated with inhibited APE1 activity, thus confirming the ability of APE1-probe to specifically detect intracellular APE1.

Similar findings were observed when reviewing the MRI images of these cells. APE1-probe-incubated cells exhibited positive contrast (brightness) and an increased T_1 MRI signal compared to the cells incubated with APE1-ir-probe. Upon inhibiting APE1 activity using the inhibitor, the T_1 MRI signal decreased, confirming the activation of APE1-probe by intracellular APE1 for MRI imaging of cancer cells (Fig. 4f, g). Similarly, T_2 MRI images displayed negative contrast

(brightness) in APE1-probe-incubated cells compared to APE1-ir-probe-incubated cells, affirming these consistent findings. The MRI results further confirmed the specificity of APE1-probe in imaging APE1 activity in cancer cells and verified the accuracy of afterglow and MRI imaging through cross-validation.

We employed APE1-activated APE1-probe for afterglow/MRI imaging radiation dose-associated APE1 expression in cancer cells (Fig. 4h). Typically, HeLa cells were exposed to various radiation doses (0, 2, 4, and 6 Gray, respectively). After 2 h, those cells were incubated with APE1-probe for 4 h. Subsequently, a series of cell samples were collected for afterglow imaging and MRI analysis. Obviously, increasing the radiation dose was positively correlated with an enhancement in the afterglow signal of cancer cells, according to afterglow images (Fig. 4i, j and Supplementary Fig. 36). Especially, at cell number of 2×10^7 cell/mL, the afterglow signal intensity was increased by 2.7-fold for 6 Gray, 2.1-fold for 4 Gray, and 1.3-fold for 2 Gray, compared to 0 Gray.

In a series of complementary experiments, we utilized HEK293 cells to represent a normal cellular context. These cells were exposed to varying levels of radiation and subsequently treated with the APE1-probe. Afterglow imaging demonstrated that the signal intensity emanating from the irradiated cancer cells was markedly higher than that from the normal cells (Supplementary Fig. 37). Furthermore, a time-course study was performed to elucidate the dynamics of afterglow emission and APE1 expression in response to radiation. The results indicated a progressive increase in afterglow luminescence from 0.5 to 4 h post radiation exposure (Supplementary Fig. 38). To quantify the cellular uptake of the APE1-probe, we employed inductively coupled plasma mass spectrometry (ICP-MS) to confirm a gradual augmentation in the internalization of the $FeMnO_x$ component of the probe (Supplementary Fig. 39).

In parallel, MRI images of cancer cells treated with different radiation dosages were obtained. The T_1 MRI images showed increased brightness as the radiation dose increased, while the T_2 MRI images became darker (Fig. 4k, l). By calculating the ΔT_1–ΔT_2 value of the MRI signal across various cell numbers (0–2×10^7 cells/mL), it was apparent that radiation dose-dependent signal differences could be identified (Fig. 4m and Supplementary Fig. 40), indicating a positive correlation between the ΔT_1 and ΔT_2 value of the MRI signal and the radiation dose. To validate the relationship between radiation dose and APE1 upregulation, western blotting was performed to measure APE1 expression within the cells following exposure to various doses (0, 2, 4, and 6 Gray) of radiation. As shown in Fig. 4n, o and Supplementary Fig. 41, the APE1 expression level gradually increased with the higher radiation doses. Those findings further corroborated the positive correlation between afterglow and MRI signals, radiation dose, and intracellular APE1 expression.

APE1-probe for afterglow/MRI imaging of radiation dose-dependent APE1 activity in tumor

In order to enhance the tumor-targeting capability of APE1-probe, we incorporate the specific tumor-targeting aptamer (AS1411) into APE1-probe. AS1411 is known for its ability to specifically recognize nucleolin, a protein that is overexpressed on the surface of cancer cells and tumor vasculature[50]. This modification allows APE1-probe with AS1411 to selectively target tumor cells. For comparison purposes, we also construct an APE1-probe (no targeting), which consisted of TA NPs-DNA4 and $FeMnO_x$-DNA2 (Fig. 5a). In this configuration, DNA4 has the same DNA sequence as DNA3 but lacks the AS1411 DNA sequence in the 3′ domain (Supplementary Fig. 23).

To evaluate their effectiveness, we intravenously injected mice bearing subcutaneous HeLa xenograft tumors with either APE1-probe or APE1-probe (no targeting). The afterglow images showed a gradual increase in afterglow luminescence at the tumor sites after injection of APE1-probe or APE1-probe (no targeting). Analysis of afterglow images revealed that the tumor injected with APE1-probe exhibited a 2.11-fold higher afterglow luminescence intensity compared to the tumor injected with APE1-probe (no targeting) at 6 h post injection (Fig. 5b, d, h and Supplementary Figs. 42, 43a), confirming the tumor-targeted imaging of APE1-probe. In addition, when comparing the afterglow imaging to the fluorescence imaging (Fig. 5b, c and Supplementary Figs. 42, 44), afterglow imaging presented a higher signal-to-noise ratio (Fig. 5i), which presented the intrinsic merit of signal-to-noise ratio for afterglow imaging. A comparative analysis of the afterglow images reveals that tumors administered with the targeted APE1-probe exhibited higher afterglow luminescence intensity than those receiving the non-targeted probe at various time points, after radiation (6 Gray) (Supplementary Fig. 45).

From the T_1 MRI images (Fig. 5j, k and Supplementary Figs. 46, 48), the T_1 MRI signal intensity of the tumor areas showed a larger increase for the tumor injected with APE1-probe (incorporating AS1411) compared to APE1-probe (no targeting) (Fig. 5o). Meanwhile, the T_2 MRI signal intensity of the tumor areas showed a larger decrease for the tumor injected with APE1-probe (Fig. 5p).

To substantiate the in vivo relationship between dose-dependent radiation and afterglow/MRI imaging, we treated the mice bearing subcutaneous HeLa xenograft tumors with radiation doses ranging from 0 to 6 Gray. After a 2-h interval, APE1-probe was intravenously injected into the treated mice, and subsequent afterglow and MRI imaging of the tumors was captured. Analysis of the afterglow images (Fig. 5d–g and Supplementary Fig. 43) revealed a gradual increase in afterglow luminescence at the tumor sites with an increase in radiation dose. Additionally, a positive correlation was observed between radiation dose and afterglow signal in tumors (Fig. 5h). Specifically, the afterglow intensity of tumors was increased by 6.8-fold for 6 Gray, 3.3-fold for 4 Gray, and 2.6-fold for 2 Gray, respectively at 1-h post injection APE1-probe. Notably, a discernible difference between 0 and 6 Gray was visible as early as 0.5 h (Fig. 5d–g), suggesting the early visualization of changes in APE1 levels during radiotherapy using APE1-probe. Subsequently, the mice were euthanized, and both the tumors and main organs were harvested for afterglow imaging (Supplementary Fig. 47). The dose-dependent afterglow signals observed in the tumor ex vivo further confirmed the reliability of APE1-probe for imaging APE1 during radiotherapy.

Next, we collected MRI images of tumors treated with varying radiation doses. Analysis of the T_1 MRI images revealed that with a radiation dose of 6 Gray, the images of tumor regions gradually brightened, and the T_1 MRI signal increased over time from 0 to 6 h (Fig. 5k–n and Supplementary Figs. 48–51). At the 6-h mark, the T_1 MRI images of the tumor exhibited an increased brightness corresponding to the elevated radiation dose, accompanied by an increase in T_1 MRI signal intensity within the tumors (Fig. 5o). Conversely, the analysis of T_2 MRI images showed a gradual darkening in the tumor and a decreasing T_2 MRI signal with an increase in radiation dose from 0 to 6 Gray. Furthermore, a comparison of T_2 MRI images of tumors treated with radiation doses of 0, 2, 4, and 6 Gray revealed increasing darkness and a decrease in signal intensity within the tumors as the radiation dose increased (Fig. 5p). These results established the correlation between afterglow MRI signals and radiation doses.

Since APE1-probe can simultaneously create positive contrast in T_1 MRI and negative contrast in T_2 MRI, this amplifies the contrast and difference between T_1 and T_2 signals within the same tumor slice. Therefore, we calculated the increased T_1 signal (ΔT_1, positive value), and increased T_2 signal (ΔT_2, negative value), and subsequently subtracted ΔT_2 from ΔT_1 to obtain ΔT_1–ΔT_2 value, thus amplifying the dynamic range and improving sensitivity. As demonstrated in Fig. 4q, the post-subtraction ΔT_1–ΔT_2 value significantly amplified the degree of MRI signal change among different radiation-treated tumors. Increasing radiation dose treatments resulted in a substantial enlargement of the subtraction comparison within the MRI signal. Notably,

https://doi.org/10.1038/s41467-024-50688-0

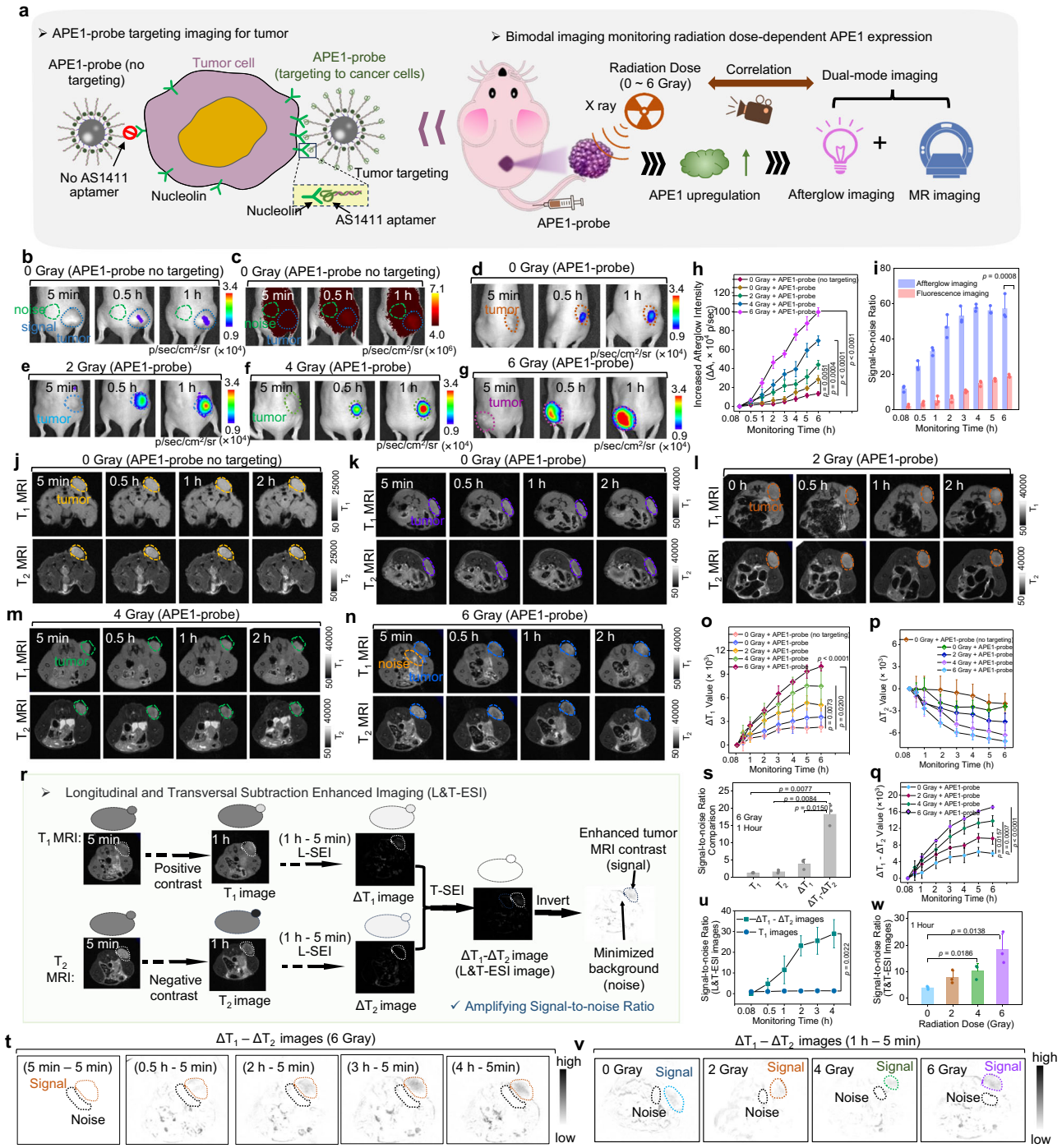

Fig. 5 | APE1-probe for afterglow/MRI imaging of radiation dose-dependent APE1 activity in tumor. a Scheme illustration of tumor-targeted imaging of APE1-probe (containing tumor-targeted AS1411 aptamer) or imaging of APE1-probe (no targeting, uncontaining AS1411 aptamer), and radiation dose-dependent afterglow/MRI imaging in vivo. **b** Afterglow imaging of mice i.v. injected with APE1-probe (no targeting) ($n = 3$ mice per group). **c** Fluorescence images of mice i.v. injected with APE1-probe (no targeting) ($n = 3$ mice per group). **d**–**g** Afterglow images of the mice treated with various radiation doses (0–6 Gray) and then intravenously injected with APE1-probe ($n = 3$ mice per group). **h** Quantified afterglow signal intensity. **i** Signal-to-noise ratio of afterglow imaging and fluorescence imaging of the mice intravenously injected with APE1-probe (no targeting). **j** T_1 and T_2 MRI images of the mice intravenously injected with APE1-probe (no targeting) ($n = 3$ mice per group). **k**–**q** The mice were treated with various radiation doses (0–6 Gray) and then i.v. injecting APE1-probe for afterglow and MRI imaging ($n = 3$ mice per group). **k**–**n** T_1 and T_2 MRI images. **o**, **p** Quantified T_1 and T_2 MRI signal intensity from (**j**–**n**). **q** Subtracted ΔT_1–ΔT_2 value of MRI signal intensity (ΔT_1: subtracted T_1 signal; ΔT_2: subtracted T_2 signal). **r** Scheme illustration and L&T-ESI images of mice with 6 Gray radiation treatment and APE1-probe injection. **s** signal-to-noise ratio comparison of MRI images before or after L&T-ESI treatment. **t**, **u** L&T-ESI images and quantification of tumor with various radiation dose treatment ($n = 3$ mice per group). **v**, **w** L&T-ESI images and quantification of mice with 6 Gray of radiation dose treatment at different time points ($n = 3$ mice per group). All afterglow imaging were obtained with white light irradiation (10 mW/cm²) time of 10 s and acquisition time of 60 s. Fluorescence imaging was obtained with excitation wavelength of 605 nm and emission of Cy5.5 channel. Data are presented as means ± SD. Statistical significance was determined using two-tailed Student's *t*-test for pairwise comparisons, and one-way ANOVA analysis of variance for multiple groups. *p* values > 0.05 were considered non-significant, while *p* values < 0.05 were considered statistically significant. Source data are provided as a Source Data file.

a distinguishable difference between 0 and 6 Gray was visible as early as the first hour through the ΔT_1–ΔT_2 MRI signal.

MRI subtraction has been reported not only to enhance MRI imaging contrast but also to improve the signal-to-noise ratio[51–53]. To enhance MRI contrast of APE1-probe for tumors, we employed a longitudinally and transversely subtraction-enhanced imaging (L&T-SEI) strategy for APE1-probe. Specifically, we planned to longitudinally subtract (L-SEI) the T_1 MRI images and T_2 MRI images at different time points to the original images for acquiring subtracted T_1 images (ΔT_1 images) and subtracted T_2 images (ΔT_2 images), respectively. These ΔT_1 and ΔT_2 images were then transversely subtracted (T-SEI) to obtain ΔT_1–ΔT_2 images using the ImageJ software (Fig. 5r and Supplementary Figs. 52).

To compare the signal-to-noise ratio among tumors treated with various radiation doses, we employed the longitudinal and transverse subtraction on the T_1 MRI images and T_2 MRI images of tumors irradiated with 6 Gray doses at 5 min and 1 h to obtain ΔT_1–ΔT_2 images (1 h−5 min) (Fig. 5r). By evaluating the aforementioned L&T-SEI images, it outlined the tumor region. We compared the signal-to-noise ratio effects induced by subtraction among T_1 images, T_2 images, ΔT_1 images, and ΔT_1–ΔT_2 images of tumors treated with a radiation dose of 6 Gray at 1 h. Notably, the signal-to-noise values for T_1 images, T_2 images, and ΔT_1 images were calculated to be 1.28 ± 0.1, 1.65 ± 0.4, and 3.86 ± 1.4, respectively. Specifically, the signal-to-noise value for ΔT_1–ΔT_2 images increased to 18.38 ± 6.0 (Fig. 5s). Thus, it was worth noticing that by eliminating background signal interference through longitudinal subtraction and emphasizing tumor signals through transverse subtraction, L&T-SEI greatly enhanced MRI contrast for the tumor and minimized background noise, thus improving the signal-to-noise ratio between the tumor and normal tissue.

Moreover, we subtracted the ΔT_1–ΔT_2 images of tumors treated with a radiation dose of 6 Gray at different time points and the analysis revealed a gradual increase in signal-to-noise values as time extended (Fig. 5t, u). Moreover, the signal-to-noise values of ΔT_1–ΔT_2 images were greatly higher than that of the corresponding T_1 images at different times. Furthermore, by calculating ΔT_1–ΔT_2 images from 1 h to 5 min, the signal-to-noise ratio with 2 Gray, 4 Gray, and 6 Gray was twofold, 2.6-fold, and 4.8-fold higher, respectively, compared to that of 0 Gray (Fig. 5v, w). This suggests that after L&T-SEI treatment, MRI images indicating APE1 changes induced by radiation doses can be observed as early as 1 h.

Afterglow/MRI imaging for early prediction of tumor radiotherapy effects

The heterogeneity of tumors and the variations among individuals in terms of demographic, racial, and genetic factors necessitate a reconsideration of the traditional one-size-fits-all approach that utilizes a maximum dose of radiation[54–57]. Therefore, the adoption of a personalized approach for radiotherapy is highly desirable to enhance treatment effectiveness and mitigate adverse effects[58,59]. This personalized therapy can be achieved via the evaluation of specific molecular biomarkers, phenotypes, or genomics associated with radiation and its toxicity[60,61]. In this work, considering the heterogeneity of tumors and individual variations of tumors, we propose combining MRI and afterglow imaging-guided radiotherapy.

The use of radiotherapy in cancer treatment is based on the generation of cytotoxic ROS and DNA damage through X-ray exposure, resulting in the apoptosis of cancer cells. To examine the production of X-ray-induced ROS and DNA damage at various radiation doses, we collected tumor samples after radiotherapy for staining purposes. Initially, the tumor slices were stained using an intracellular ROS indicator called 2′,7′-dichlorofluorescein diacetate (DCFH-DA). By analyzing confocal images and corresponding quantification results (Fig. 6b, c), we observed a progressive increase in fluorescence signal in the tumor slices with higher radiation doses. This finding suggested that higher radiation doses enhance ROS generation within tumors. Subsequently, we assessed intratumor DNA damage levels through immunofluorescence analysis utilizing H_2AX antibody staining on tumor slices. Analysis of confocal images and corresponding quantification (Fig. 6d, e) indicated that higher radiation doses led to elevated fluorescence signals, indicating more severe DNA damage. Given that intratumor DNA damage and ROS production stimulate the upregulation of APE1, which served to balance the intracellular redox environment and facilitate DNA repair, we stained the tumor slices with an APE1 antibody to test its expression. The confocal images and quantification results shown in Fig. 6f, g demonstrated a gradual increase in fluorescence signal within tumor slices as the radiation dose increased from 0 to 6 Gray, confirming the radiation dose-dependent upregulation of APE1.

Subsequently, we monitored the growth of the tumors by subjecting mice with HeLa tumors to different radiation doses (0, 2, 4, and 6 Gray) and tracking tumor growth over 12 days. Analysis of the tumor growth curves and measurements of tumor weight taken at day 12 post-irradiation (Fig. 6h, i and Supplementary Fig. 53) revealed that a radiation dose of 2 Gray induced partial inhibition of tumor growth compared to the control group. Treatment with 4 Gray of radiation resulted in even greater inhibition of tumor growth, while 6 Gray of radiation significantly suppressed tumor growth. Additionally, histological damage observed in the H&E-stained and TUNNEL images further corroborated the finding that higher radiation doses were associated with more pronounced therapeutic outcomes (Fig. 6j, k), supporting the notion of a radiation dose-dependent response.

Next, we created a heating map for those parameters. The heating map showed a good positive correlation between radiation dose and the enhancement of afterglow and MRI signals in the APE1-probe, as well as the increased ROS generation, intratumor DNA damage, and APE1 expression (Fig. 6l). It meant that the afterglow and MRI imaging can track the dynamic levels of APE1 during radiotherapy, which is benefited for evaluating ROS production, intratumor DNA damage, and predicting therapeutic outcomes (Fig. 6a). Moreover, our findings indicated that afterglow and MRI imaging can detect changes in APE1 levels as early as 3 h after irradiation, whereas therapeutic outcomes based on tumor size can only be observed after ~6 days. This highlights the potential utility of early APE1 detection in predicting radiotherapy outcomes. Future investigations could focus on exploring the probe's potential to guide personalized radiotherapy strategies and enhance therapeutic efficacy.

Afterglow/MRI imaging of APE1 activity in radiation-induced liver injury

It is important to acknowledge that there is a potential side effect of radiation therapy known as radiation-induced liver organ injury, which refers to the damage inflicted upon liver tissue during the course of treatment[62,63]. This injury can lead to the development of diseases such as hepatitis, fibrosis, cirrhosis, and even cancer[64]. Therefore, it becomes crucial to diagnose and monitor liver injury to effectively manage and intervene[65].

However, due to the intricate structure of the liver and its involvement in multiple physiological processes, identifying early signs of liver organ injury can be quite challenging[66]. In the initial stages, liver organ injury often manifests itself through general symptoms like fatigue, nausea, or loss of appetite, which can easily be attributed to other causes or even the cancer itself[67]. The absence of specific symptoms adds another layer of complexity to the situation, making it difficult to differentiate between liver organ injury and other conditions[67]. Additionally, symptoms of liver organ injury may not present themselves immediately after radiation therapy, sometimes taking several weeks or even months to emerge[62,63,68]. The timing of symptoms can vary based on a variety of factors such as radiation dosage, fractionation, and individual patient characteristics[63,68].

https://doi.org/10.1038/s41467-024-50688-0

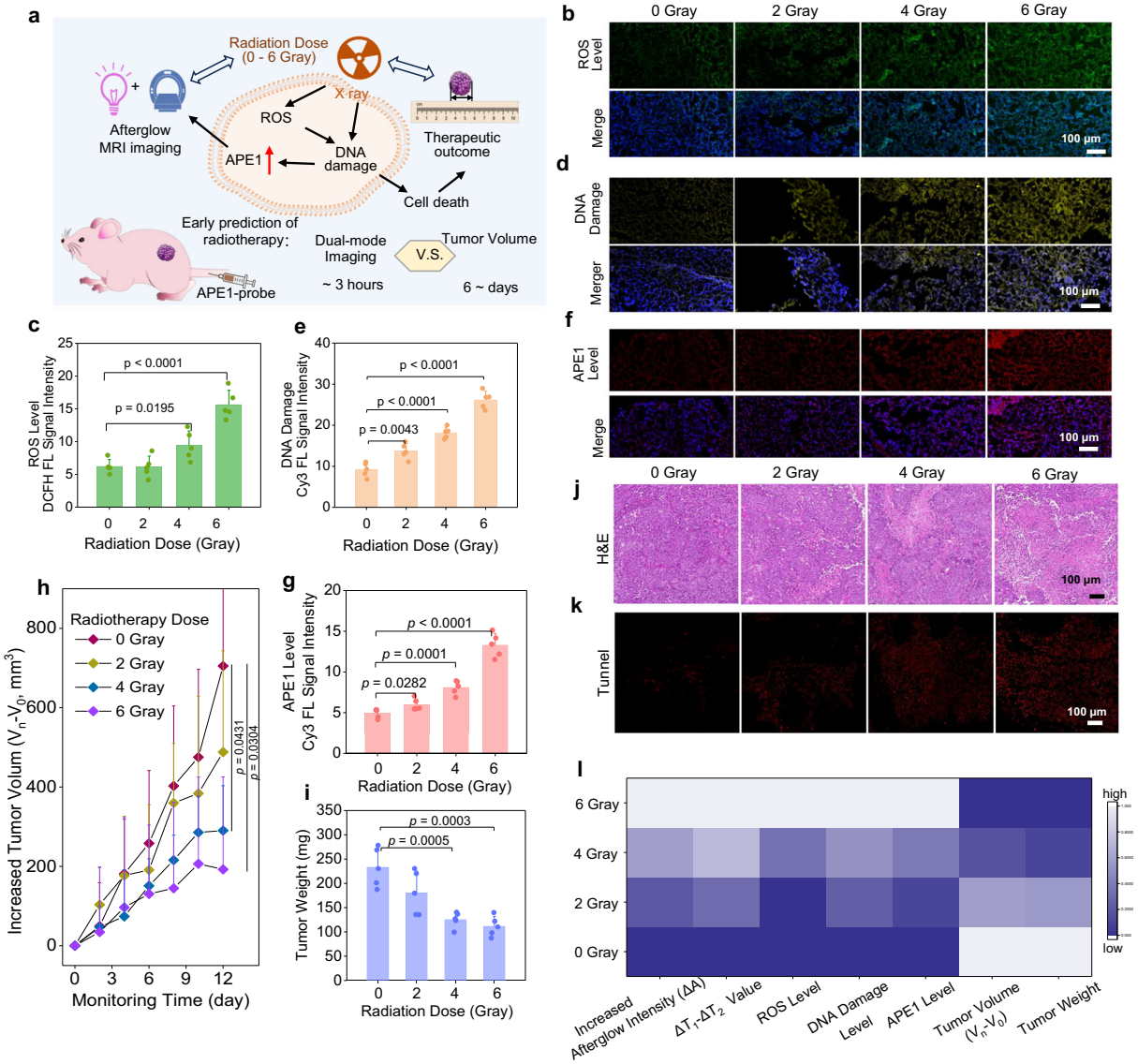

Fig. 6 | Afterglow/MRI imaging for early prediction of tumor radiotherapy effects. a Scheme illustration. **b**–**g** Fluorescence confocal images and signal intensity for immunofluorescence of tumors slice with treatment various radiation does (0–6 Gray) ($n = 5$ mice per group). **b**, **c** Tumor slice staining with DCFH-DA for testing ROS yield. **d**, **e** Tumor slice incubating with H_2AX antibody and Cy3-labeled IgG for testing DNA damage ($n = 5$ mice per group). **f**, **g** Tumor slice incubating with anti-APE antibody and Cy3-labeled IgG for testing APE1 level ($n = 5$ mice per group). **h**, **i** Nude mic bearing subcutaneous HeLa xenograft tumors with various radiotherapy doses during the 12 days of observation ($n = 5$ mice per group). **h** Tumor growth curves. **i** Tumor weight. **j**, **k** Representative images of H&E-stained and tunnel immunofluorescence of tumor slice treated with various radiotherapy doses. **l** Correlation between radiotherapy and afterglow/MRI signal intensity for early prediction of therapeutic outcome ($n = 5$ mice per group). Data are presented as means ± SD. Statistical significance was determined using two-tailed Student's *t*-test for pairwise comparisons, and one-way ANOVA analysis of variance for multiple groups. *p* values > 0.05 were considered non-significant, while *p* values < 0.05 were considered statistically significant. Source data are provided as a Source Data file.

Imaging modalities like ultrasound and computed tomography may lack the sensitivity required to detect early signs of liver organ injury, especially in instances of subtle or localized liver organ damage[69].

We proposed the afterglow/MRI imaging of APE1-probe to evaluate APE1 level in liver organ injury. Firstly, we irradiated the liver region of nude mice with varying doses of X ray radiation (ranging from 0 to 6 Gray). After 2 h, all mice received an intravenous injection of APE1-probe for afterglow and MRI signal detection. The afterglow images clearly showed a gradual enhancement of the afterglow signal in the liver area as the radiation dose increased (Fig. 7b, c). Specifically, at 4 h post injection of APE1-probe, the afterglow intensity increased by 4.2-fold for 2 Gray, 6.5-fold for 4 Gray, and 8.1-fold for 6 Gray. Moreover, at 8 h post injection of APE1-probe, the liver organs were harvested from each group for afterglow imaging. The afterglow images of the liver organs demonstrated a positive correlation between the afterglow signal intensity and the radiation dose (Fig. 7d, e). These results indicated that afterglow imaging could more sensitively report the radiation-induced APE1 level change in the liver, even at 2 Gray of radiation. Notably, the change in afterglow signal could be detected as early as 2 h post injection of APE1-probe (4-h post radiation treatment), providing a much earlier detection time window.

MRI is a high-resolution clinical diagnostic technology that can provide clear anatomical structure visualization[36,70]. Since APE1-probe can provide molecular information on APE1 levels using MRI (indicating functional MRI), combined with anatomical MRI, APE1-probe can offer both anatomical and functional imaging, enabling the precise identification of injury regions within the liver (Fig. 7a). In our study, we obtained MRI images of the liver region treated with varying radiation

https://doi.org/10.1038/s41467-024-50688-0

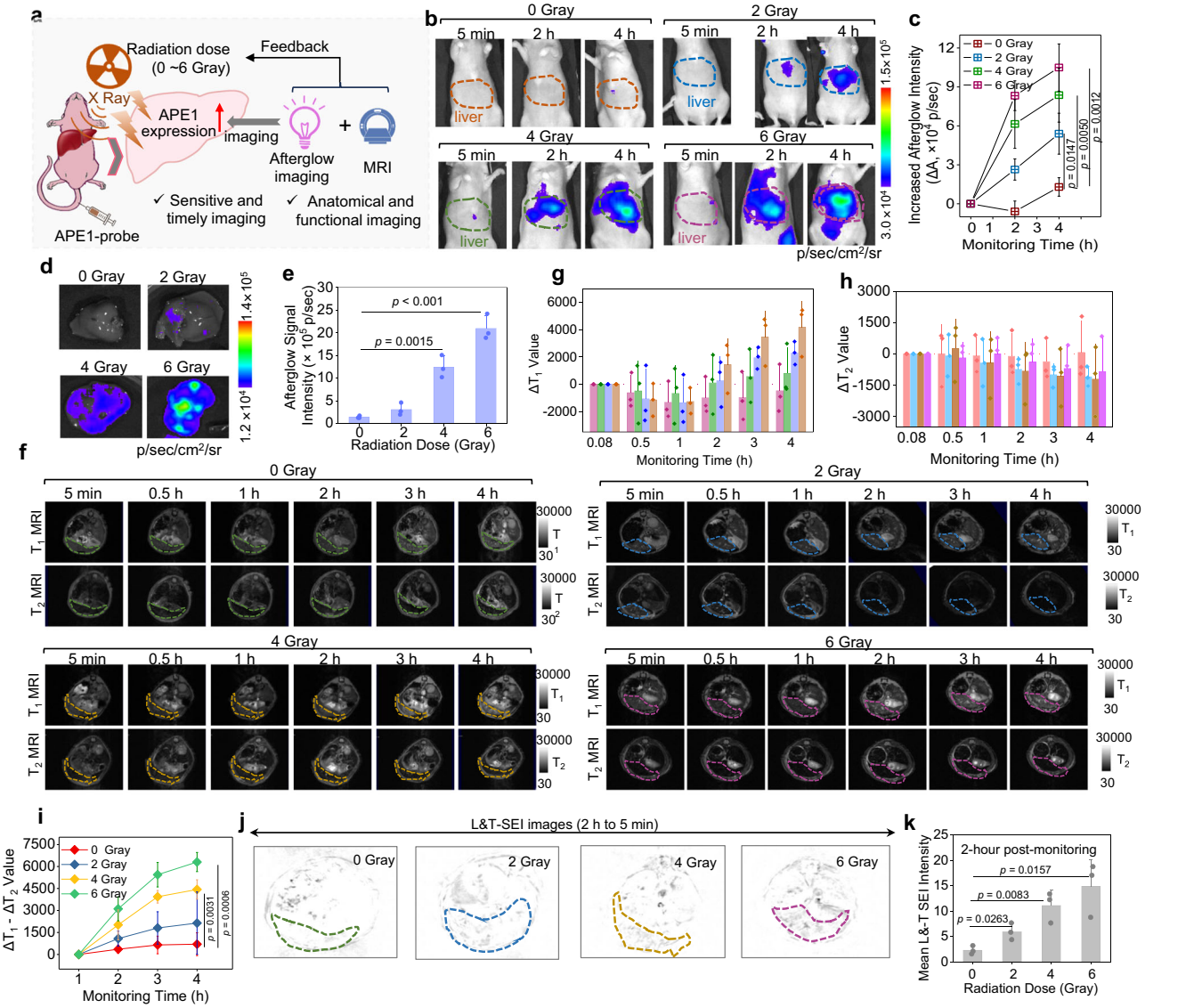

Fig. 7 | Afterglow/MRI imaging of APE1 activity in radiation-induced liver injury. a Scheme illustration for APE1-activated afterglow/MRI imaging for evaluating radiation-induced liver organ injury. **b**–**i** Liver region of mice was treated with various radiation dose (0–6 Gray) and then injected with APE1-probe ($n = 3$ mice per group). **b**, **c** Afterglow luminescence images and increased signal intensity. **d**, **e** Afterglow images and signal intensity of in-vitro liver organ after injection of APE1-probe for 8 h. **f** T_1 MRI and T_2 MRI images of liver region of mice treated with various radiation dose (0–6 Gray). **g**, **h** Increased T_1 MRI intensity and decreased T_2 MRI intensity. **i** Subtracted MRI signal intensity (ΔT_1–ΔT_2 value). **j** L&T-SEI images of the liver region with various radiation treatment (at 2-h post-monitoring) ($n = 3$ mice per group). **k** Quantified signal intensity of L&T-SEI images (ΔT_1–ΔT_2 value), data from (**j**). All afterglow images were obtained with a white light irradiation (10 mW/cm²) time of 10 s and an acquisition time of 60 s. Data are presented as means ± SD. Statistical significance was determined using two-tailed Student's *t*-test for pairwise comparisons, and one-way ANOVA analysis of variance for multiple groups. *p* values > 0.05 were considered non-significant, while *p* values < 0.05 were considered statistically significant. Source data are provided as a Source Data file.

doses (Fig. 7f and Supplementary Fig. 54) and calculated ΔT_1 (positive value) or ΔT_2 (negative value). T_1 MRI images of the liver illuminated and ΔT_1 signal of tumor areas increased over time, with increasing radiation doses (Fig. 7f, g). Conversely, T_2 MRI images showed gradual darkness in the tumor as the radiation dose increased (Fig. 7f). By comparing T_2 MRI images of tumors treated with different radiation doses, we observed that higher doses resulted in lower signal intensity in the liver region (Fig. 7h).

To amplify the contrast between T_1 MRI and T_2 MRI images at the same liver slice for improving sensitivity, we subtracted ΔT_2 from ΔT_1, obtaining ΔT_1–ΔT_2 (Fig. 7i). As the irradiation dose increased, the value of ΔT_1–ΔT_2 increased, indicating a good relationship between MRI signal and X-ray dose. This subtraction significantly increased the change range of MRI signals among different radiation doses.

Furthermore, to enhance the MRI image contrast between the liver region and normal tissue, we employed the L&T-SEI strategy to distinct the MRI images of the liver region treated with different radiation doses at 2-h post injection of APE1-probe (Fig. 7j). The mean L&T-SEI intensity gradually enhanced with the X-ray dose increased (Fig. 7k). Therefore, APE1-probe for afterglow and MRI imaging can detect subtle changes in APE1 level in the radiation-treated liver as early as 2 h post injection of the probe.

To analyze radiation-induced ROS yield, DNA damage, and APE1 upregulation in liver tissue, we harvested liver tissue at 6 h post injection of APE1-probe for sectioning and various staining. The fluorescence confocal images of liver slices stained with DCFH-DA revealed increased fluorescence intensity with higher radiation doses, implying enhanced ROS generation (Fig. 8b, c). Staining liver slices

https://doi.org/10.1038/s41467-024-50688-0

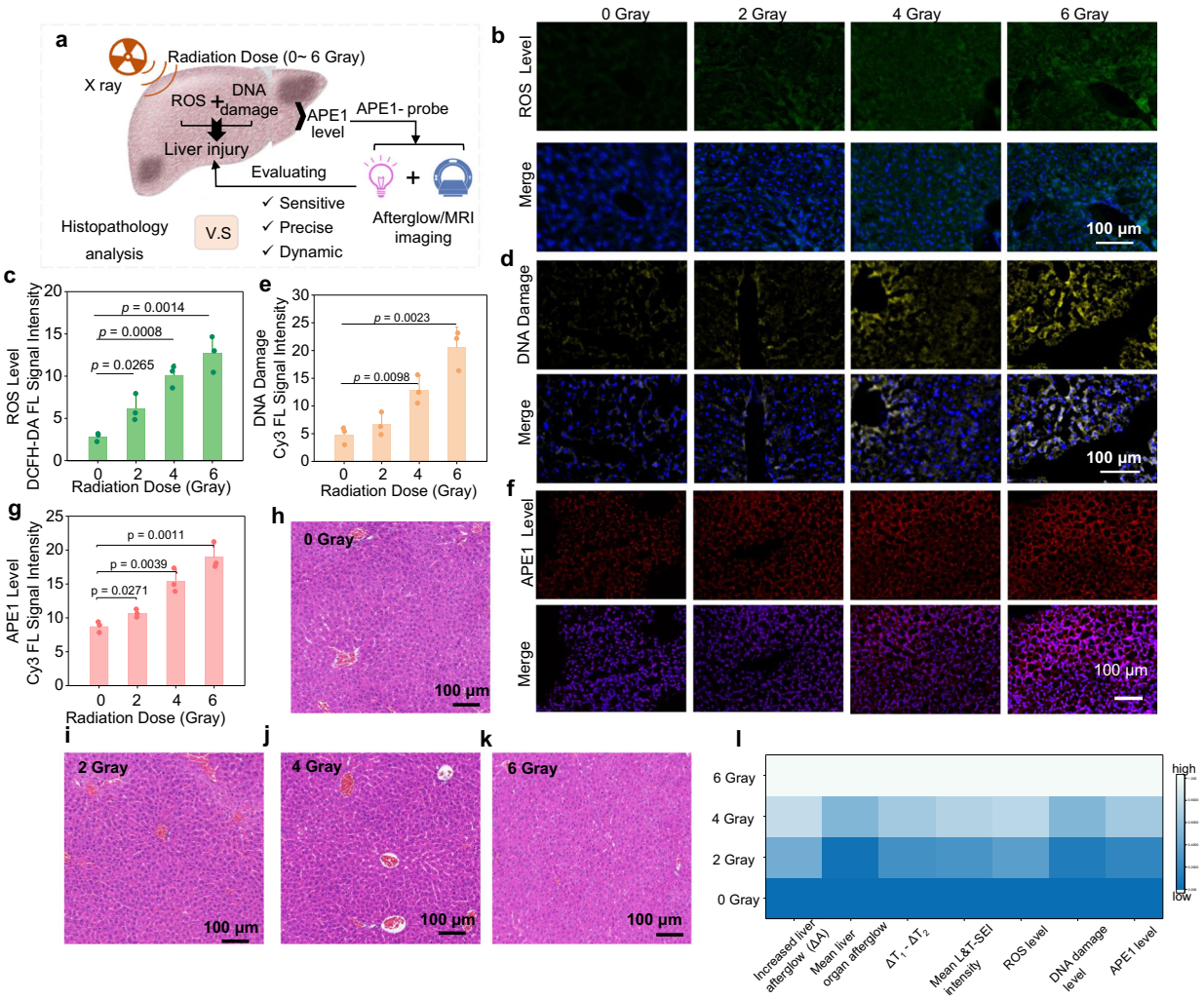

Fig. 8 | Determination of radiation-induced liver injury. a Scheme illustration for APE1-activated afterglow/MRI imaging for evaluating radiation-induced liver organ injury. **b**, **c** Liver slice staining with DCFH-DA for testing ROS yield ($n = 3$ mice per group). **d**, **e** Liver slice incubating with H_2AX antibody and Cy3-labeled IgG for testing DNA damage ($n = 3$ mice per group). **f**, **g** Liver slice incubating with anti-APE antibody and Cy3-labeled IgG for testing APE1 level ($n = 3$ mice per group). **h**–**k** Representative H&E staining analysis of liver treated with various radiation dose (0–6 Gray) ($n = 3$ mice per group). **l** Correlation between radiate on does, afterglow/MRI signal intensity, ROS generation, DNA damage level and APE1 level ($n = 3$ mice per group). Data are presented as means ± SD. Statistical significance was determined using two-tailed Student's *t*-test for pairwise comparisons, and one-way ANOVA analysis of variance for multiple groups. *p* values > 0.05 were considered non-significant, while *p* values < 0.05 were considered statistically significant. Source data are provided as a Source Data file.

with H_2AX antibody showed more severe DNA damage in response to higher radiation doses (Fig. 8d, e). Additionally, APE1 levels in the liver exhibited a radiation dose-dependent increase (Fig. 8f, g). Furthermore, pathological analysis of liver organ tissue using H&E staining was performed. Interestingly, no significant evidence of liver organ injury was observed when radiation doses ranging from 0 to 6 Gray were administered (Fig. 8h–k). These findings suggest that H&E staining alone lacks the necessary sensitivity to detect liver organ injury at early stages and under low-dose X-ray radiation. Furthermore, biochemical assay results revealed a dose-dependent increase in alanine aminotransferase (ALT), aspartate aminotransferase (AST), total bilirubin (TBIL), and total bile acids (TBA) (Supplementary Fig. 55).

Next, we created a heat map that showed a good correlation between, afterglow/MRI signal intensity, radiation dose, ROS generation, DNA damage level, and APE1 level in the liver, it was evident that all tested parameters were dose-dependent (Fig. 8l). Based on the strong correlation among these parameters, APE1-probe for afterglow and MRI imaging can monitor the dynamic level of APE1 during radiation-induced liver injury. Additionally, significant changes in APE1 level in the liver can be detected as low as 2 Gray of radiation and as early as 2 h via afterglow imaging and MRI, which showed more sensitivity compared with histopathology analysis (H&E staining), showcasing its potential utility in assessing radiation-induced liver damage early on. Thus, this advancement holds significant promise for informing treatment responses to radiotherapy and its toxicity.

MRI imaging of APE1 activity in radiation-induced abscopal effect

Radiation therapy is known to induce oxidative stress and DNA damage not only in irradiated tumors but also in neighboring unirradiated tumors, referred to as the radiation-induced abscopal effect[71,72]. The abscopal effect has potential benefits in tumor control as it can cause damage to neighboring cancer cells that were not directly irradiated, enhancing the overall effectiveness of radiation therapy[72,73]. Additionally, the release of signaling molecules and immune modulators from irradiated cells can stimulate the immune system and promote an anti-tumor immune response, potentially improving tumor control and outcomes in tumors receiving both radiation therapy and immunotherapy[74]. Despite these promising aspects, there

https://doi.org/10.1038/s41467-024-50688-0

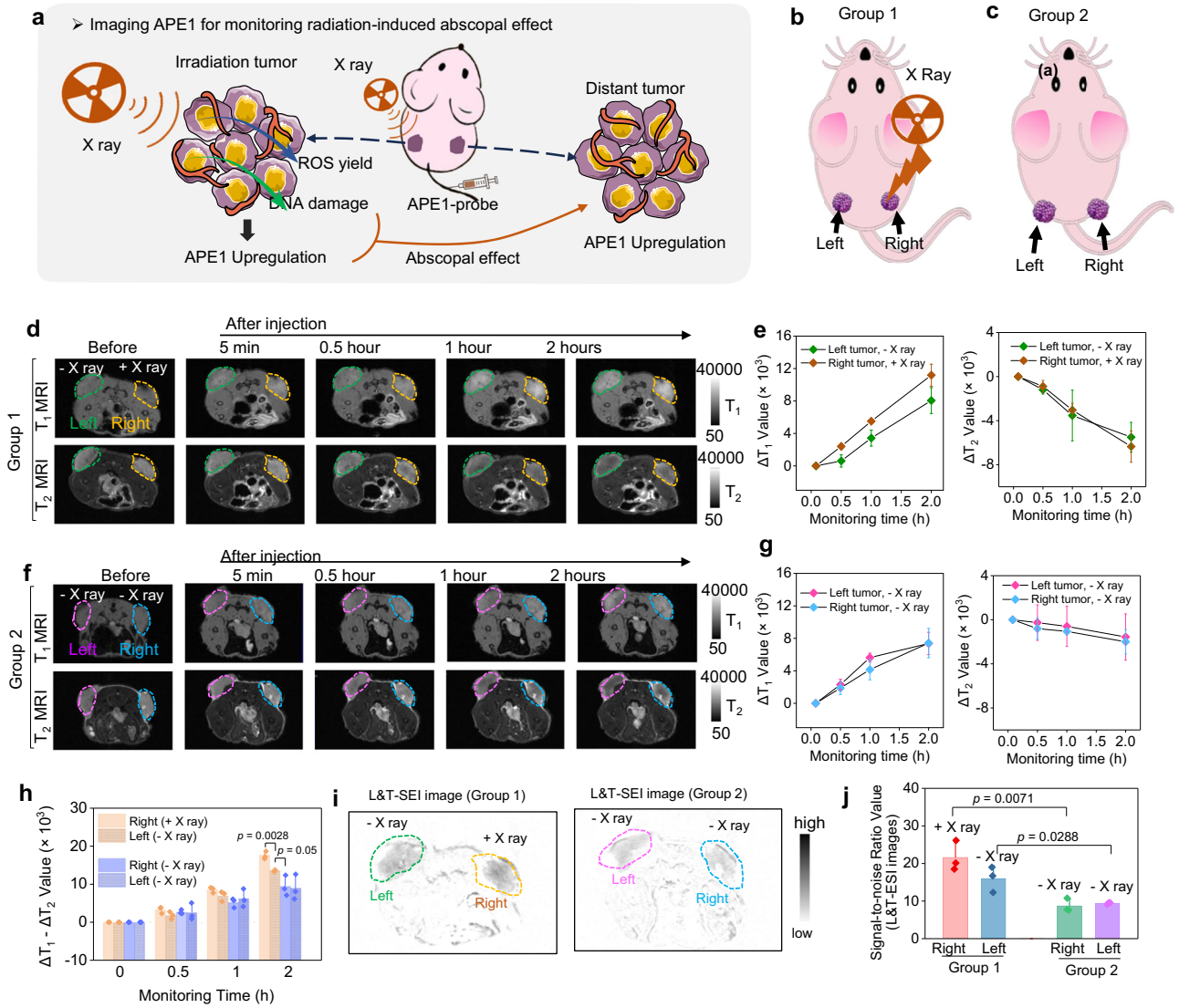

Fig. 9 | MRI imaging of APE1 activity in radiation-induced abscopal effect. **a** Scheme illustration. **b** Scheme illustration of the Group 1 mice with radiation treatment only in right tumor and then intravenous injection of APE1-probe. **c** Scheme illustration of the Group 2 mice with intravenous injection of APE1-probe. **d** MRI images of the Group 1 mice with radiation treatment only in right tumor and then intravenous injection of APE1-probe ($n = 3$ mice per group). **e** Increased T_1 MRI intensity and decreased T_2 MRI intensity for Group 1. **f** MRI images of the Group 2 mice with intravenous injection of APE1-probe ($n = 3$ mice per group). **g** Increased T_1 MRI intensity and decreased T_2 MRI intensity for Group 2. **h** ΔT_1–ΔT_2 signal value from (**e**, **g**). **i** L&T-SEI images from Group 1 and Group 2 at 2-h post-monitoring. **j** Signal-to-noise ratio from (**i**). Data are presented as means ± SD. Statistical significance was determined using two-tailed Student's *t*-test for pairwise comparisons, and one-way ANOVA analysis of variance for multiple groups. *p* values > 0.05 were considered non-significant, while *p* values < 0.05 were considered statistically significant. Source data are provided as a Source Data file.

are challenges in understanding the complex interactions between radiation and the immune system[74].

In this part, we employed APE-probe for imaging of APE1 activity in radiation-induced abscopal effect (Fig. 9a). We established the nude mice model bearing two subcutaneous HeLa xenograft tumors and selectively irradiated the right tumor with 6 Gray (right tumor of Group 1, +X ray) while completely shielding the left tumor from X-ray irradiation (left tumor of Group 1, −X-ray) (Fig. 9b). Two hours after irradiation, we administered an intravenous injection of APE1-probe to the mice in Group 1 for MRI imaging. As a control, nude mice with right and left tumors received no X-ray radiation and were injected with APE1-probe (right and left tumors of Group 2, -X-ray) (Fig. 9c). From the T_1 MRI images (Fig. 9f, g, and Supplementary Fig. 56), we observed that when both tumors on the same mice received no irradiation (Group 2), there was no discernible difference in MRI contrast and signal between the right and left tumors. In contrast, irradiation of the right tumor with X-ray resulted in increased brightness not only in the irradiated tumor but also in the non-irradiated left tumor on the same mice (Group 1) (Fig. 9d, e, and Supplementary Fig. 57). Correspondingly, T_2 MRI images demonstrated a reverse change in MRI signal compared to T_1 MRI images. Next, we calculated the ΔT_1–ΔT_2 value of MRI signal intensity for each tumor. At 2 h post injection of APE1-probe, we found that radiation improved the ΔT_1–ΔT_2 MRI signal of the right tumor that received radiation (right tumor of Group 1, +X-ray), as well as elevating the MRI signal of the left tumor that received no X-ray radiation treatment in (left tumor of Group 1, −X-ray). In contrast, no discernible difference in ΔT_1–ΔT_2 MRI signal was observed for both the right and left tumors in Group 2, when no X-ray radiation was applied to the mice (Fig. 8h).

To amplify the signal change, we employed MRI subtraction by longitudinally and transversely subtracting the T_1 and T_2 MRI images in 2-h monitoring periods to obtain ΔT_1–ΔT_2 images. As illustrated in

Fig. 9i, j, this approach efficiently removed background signal interference, resulting in a substantial enhancement of MRI contrast for tumors. By comparing the signal-to-noise ratio (tumor to normal tissue), we observed that the irradiation not only enhanced the APE1 level in the irradiated tumor (right tumor of Group 1, +X-ray) but also in the non-irradiated tumor on the same mouse (left tumor of Group 1, −X-ray). The afterglow images revealed a marginal increase in the afterglow signal for the irradiated right tumor relative to the non-irradiated left tumor (Supplementary Fig. 58). Additionally, immunohistochemical fluorescence analysis corroborated an upregulation of APE1 expression in the irradiated tumor (Group 1, +X ray) in contrast to the non-irradiated tumor (Group 1, −X-ray) (Supplementary Fig. 59). Consequently, this probe can effectively detect the upregulation of APE1 in tumors adjacent to radiation-treated tumors, which provides a tool to gain insights into the underlying mechanisms and develop strategies to maximize their synergistic effects.

Methods

Ethical statement

All research complied with all relevant ethical regulations: in an adult mouse with a single tumor, the mean diameter of the tumor (measured by $(L \times W^2)/2$) must not exceed 15 mm. For studies where two tumors are grown on contralateral flanks on one animal, the size of these should be less and should not exceed the maximum burden of a single tumor. The animal experiments are conducted following the principles of Laboratory Animal Care and the guidelines of the Institutional Animal Care and Use Committee of Hunan University (SYXK 2022-0007 (Xiang)). Nude mice (female, 4–6 weeks old) are obtained from Hunan SJA Laboratory Animal Co. Ltd (Changsha, China). All mice (5 mice per cage) are housed in a specific pathogen-free environment with a light cycle of 12 h:12 h at a temperature of 18–22 °C and a humidity of 50–60%. All mice are promptly euthanized using CO_2 gas after finishing the animal experiment.

Materials. Polymethacrylates (PSMA, M_w = ~2000), pluronic-F127 (F127, M_w = ~12,600), poly[2,7-(9,9′-dioctylfluorene)-alt-4,7-bis(thiophen-2-yl) benzo-2,1,3-thiadiazole] (PFODBT, M_w = 10,000 ~ 50,000), and poly[2-methoxy-5-(2-ethylhexyloxy)-1,4-phenylenevinylene] (MEHPPV, M_w = 40,000 ~ 70,000) are purchased from Sigma-Aldrich (USA). 1,2-dimyristoyl-sn-glycero-3-phosphoethanolamine-N-[methoxy (polyethylene glycol)] (DSPE-PEG, M_w = 2000) are obtained from ToYong Bio Tech. Inc. (Shanghai, China). Iron chloride ($FeCl_3{\cdot}6H_2O$, 99%), erucic acid (80%), manganous chloride ($MnCl_2{\cdot}4H_2O$, 99%), oleic acid (96%), ascorbic acid (AA, 99%), sodium hydroxide (NaOH, 97%), copper sulfate ($CuSO_4$, 99%), 1-(3-Dimethylaminopropyl)-3-ethyl carbodiimide hydrochloride (EDC) are purchased from Aladdin Chemical Ltd (Shanghai, China). Oxhydryl-poly (ethylene glycol)-azide (HO-PEG-N_3, Mw = 2000 Da) was purchased from Ponsure Biological Tech. Inc. (Shanghai, China). Phosphoryl chloride ($POCl_3$) is purchased from Energy Chemical (Shanghai, China) Co., Ltd. Tris-hydroxylpropyl triazolylamine (THPTA, >98%) is bought from Glen Research (USA). 2-bromo-2-methylpropionic acid (BMPA) is purchased from Sahn Chemical Technology Co., Ltd (Shanghai, China). Sodium carbonate (Na_2CO_3, AR), hydrochloric acid (HCl, GR), sodium chloride (NaCl, AR), magnesium chloride ($MgCl_2{\cdot}6H_2O$, AR) ethanol (AR), hexane (AR), tetrahydrofuran (AR), chloroform (AR), N, N-dimethylformamide (AR), and petroleum ether (AR), are purchased from Sinopharm Chemical Reagent Co., Ltd (Shanghai, China). Dulbecco's modified eagle medium (DMEM), fetal bovine serum (FBS), and penicillin-streptomycin are obtained from Gibco, Life Technologies (USA). APE1 primary antibody is purchased from Abcam (UK). H_2AX primary antibodies, HRP, or Cy3-conjugated secondary antibodies are purchased from Beyotime (Shanghai, China) Biotechnology Co., Ltd. Dulbecco's phosphate-buffered saline (DPBS) is obtained from Thermo Fisher Scientific (USA). Trypsin/EDTA (0.25%) is purchased from Hyclone. 2′,7′-dichlorofluorescin diacetate (DCFH-DA, >97%) is purchased from bought from Sigma-Aldrich (Shanghai, China). APE1 enzyme and 10× Nebuffer are purchased from New England Biolabs (NEB, USA). CRT0044876 inhibitor is purchased from Med Chem express (MCE, USA). Human embryonic kidney cell lines (HEK293 cells) and Human cervical cancer cell lines (HeLa cells) are obtained from the National Collection of Authenticated Cell Cultures (Shanghai, China). All DNAs are obtained from Sangon Biotech Co., Ltd (Shanghai, China) with HPLC-CE purification. Water (18.2 MΩ) is purified by the Milli-Q Direct-8 water purification system (Millipore).

The DNA sequences (from 5′ to 3′) of the involved oligonucleotides are listed in as follows:

DNA1 (amino): 5′-NH_2-AAAAAATATCGATG/idsp/GT*T*A*G*C*G*A-3′

DNA2 (alkyne): 5′-G*G*T*G*G*T*GGTGGTTGTGGTGGTGGTGGTC GCTAACCCATC GATAAAAA-alkyne-3′

DNA3 (amino): 5′-NH_2-AAAAAATATCGATGGGT*T*A*G*C*G*A-3′

DNA4 (alkyne): 5′-C*G*C*T*A*A*CCCATCGATAAAAA-alkyne-3′

(*stands for phosphorothioate bonds)

Characterization. Transmission electron microscopy (TEM) and energy dispersive X-ray (*EDX*) analysis are performed by JEM-2100F (JEM-2010, JEOL, Japan) with an accelerating voltage of 200 kV. Dynamic light scattering (DLS) measurements are performed on a Zetasizer Nano ZS90 (Malvern) with a 90° scattering angle and a He-Ne laser. The absorbance is measured by UV-vis spectrophotometer (UV-1800, Shimadzu). Fluorescence spectra and afterglow luminescence spectra are collected by Edinburgh Instruments F-S5 fluorescence spectrometer. The transverse relaxation time is measured on a Bruker Minispec analyzer (60 MHz, Bruker, Germany). X-ray diffraction (*XRD*) measurement is performed on a XRD6100 (Rigaku) X-ray diffractometer. X-ray photoelectron spectroscopy (*XPS*) analysis is conducted on Thermo Scientific K-Alpha (ThermoFisher Scientific, USA). Fourier-transformed infrared (FTIR) spectroscopy is performed using a Fourier Transform Infrared Spectrometer (FOLI20). Magnetic resonance imaging and mapping imaging are performed with a 7T MRI scanner (Pharma Scan 70/16 US, Bruker). Afterglow luminescence and fluorescence imaging of solution or animal are performed using an IVIS Lumina XR imaging system under bioluminescence (no excitation) and fluorescence modes, respectively. The amount of metallic element is measured by inductively coupled plasma-mass spectrometry (ICP-MS, 8900, Agilent). Radiation treatment is arranged using RS 2000 Small Animal Irradiator. The lead plate with thickness of 1 cm was used for shielding against X-ray radiation of 6 Gray (shielding efficiency to be nearly 100%). Living Image® software (IVIS imaging systems) was used to analyze afterglow signal and fluorescence data. Para Vision 360 software was used to analyze MRI signal data. Image J software was used to subtract MRI images and analyze subtraction MRI data, immunofluorescence data, and western blotting data. Data was represented by Origin2018 and Excel.

Programmed self-assembly for APE1-activated core-satellite nanoprobe

Synthesis of TA. The synthesis procedure is depicted in Supplementary Fig. 1[39]. To synthesize Compound **1**, a solution of 3,6-dibromonaphthalene-2,7-diol (15.0 g, 47 mmol) in a mixture of methanol (600 mL) and water (1.8 L) in a volumetric ratio of 1:3 is subjected to dropwise addition (one drop per second) of 0.05 M $KMnO_4$ (1.86 g, 11.7 mmol), followed by stirring for 36 h at room temperature. The progression of the reaction was monitored using TLC to ensure the complete consumption of the starting material. Once the reaction reached completion, it was terminated by adding 1 M HCl (pH = 2). Precipitates were obtained through filtration and subsequent washing with water. The resulting residue was then purified via recrystallization

from methanol, yielding compound 1 (14.4 g, 97% yield) in the form of a dark solid.

To synthesize Compound **2**, a solution of compound **1** (3.00 g, 4.8 mmol) in methanol was treated with $Na_2S_2O_4$ (3.33 g, 19.2 mmol) under an argon atmosphere and stirred for 48 h at room temperature. The progress of the reaction was monitored using TLC to confirm the consumption of the starting material. Upon completion, the reaction was quenched by the addition of 1 M HCl (pH = 2). Following filtration, the residue was washed with water and dried, resulting in a yellow crude Compound **2** (2.90 g) obtained without further purification for the subsequent step.

To synthesize Compound **3**, a solution of compound **2** (300 mg, 0.48 mmol) in dry dioxane and tetrabutylammonium bromide (2.24 g, 3.84 mmol), KOH (160 mg, 2.88 mmol), *n*-Butyl bromide (5 mL) was added at room temperature. The mixture then was slowly warmed up to 80 °C and stirred for 48 h. Upon completion, the solution was extracted with water (50 mL) and ethyl acetate (50 mL). The organic section was dried by anhydrous $MgSO_4$. After filtration, the organic layer was evaporated for dryness. The residue was purified by column chromatography on silica gel (petroleum ether) to afford compound **3**.

To synthesize Compound **4**, Compound **3** (1.0 g, 1.2 mmol) was dissolved in dry DMF (50 mL) under an argon atmosphere, and CuI (1.4 g, 7.2 mmol) was added. Then, a solution of MeONa in methanol (42.5 mL, 12 mmol) was added dropwise (one drop per second). The resulting mixture was stirred at 120 °C, and the progress of the reaction was monitored by thin-layer chromatography (TLC) to ensure the consumption of the starting material. After completion, the reaction was stopped with water, extracted with dichloromethane (250 mL), and dried with $MgSO_4$. The solvent was removed, and the residue was purified by silica gel chromatography (petroleum ether: dichloromethane = 3:2) to yield compound **4** (601 mg, 76%) as a green-yellow solid.

For the synthesis of Compound **5**, Compound **4** (200 mg, 0.30 mmol) was dissolved in dichloromethane (80 mL) under an argon atmosphere at −78 °C. N-bromosuccinimide (NBS) (0.60 mmol, 108 mg) was then added gradually. The reaction progress was monitored by TLC to ensure the consumption of the starting material. After reaction completion, the mixture was incubated to room temperature and diluted with dichloromethane (20 mL) and water (15 mL). The organic layer was dried with anhydrous $MgSO_4$. The solvents were evaporated, and the residue was purified by silica gel chromatography (petroleum ether: dichloromethane = 5:1) to obtain compound **5** (100 mg, 41%) as a yellow solid.

To synthesize Compound **6**, compound **5** solution (0.12 mmol, 100 mg) in dry toluene (25 mL) was prepared. To this solution, Pd$(PPh_3)_4$ (0.012 mmol, 14 mg), 2-formylphenylboronic acid (0.24 mmol, 37 mg), and aqueous solution K_2CO_3 (2 M, 5 mL) were added under an argon atmosphere. The mixture was stirred at 80 °C, and TLC was used to monitor the progress of the reaction. Upon completion, the organic layer was dried with anhydrous $MgSO_4$. After removing the solvents, the residue was purified by silica gel chromatography (petroleum ether: dichloromethane = 2:1) to yield compound **6** as a yellow solid.

For the synthesis of afterglow molecules (TA), a solution of compound **6** (0.08 mmol, 70 mg) in dry tetrahydrofuran (50 mL) was prepared, and 2-mesitylmagnesium bromide (1 M in THF, 1 mL) was added slowly. The mixture was stirred at room temperature, and TLC was employed to monitor the reaction progress. After completion, the reaction was stopped with water, extracted with dichloromethane (150 mL), and the organic layer was dried with anhydrous $MgSO_4$. After removing the solvent, the crude diol, without further purification, was used directly for the next step. The diol was dissolved in dry dichloromethane (30 mL), and boron trifluoride etherate (0.10 mL, 0.32 mmol, 4.00 equiv.) was added slowly. The reaction progress was monitored by TLC. Upon completion, the reaction was quenched with H_2O (8 mL), extracted with dichloromethane, and dried with $MgSO_4$ to yield the residue. The residue was dissolved in toluene, and 2,3-dichloro-5,6-dicyano-1,4-benzoquinone (DDQ) (27 mg, 0.16 mmol) was added, followed by stirring for 0.5 h. Toluene was evaporated, and the residue was purified by silica gel chromatography (petroleum ether: dichloromethane = 10:1) to yield compound TA (63 mg, 73% in two steps) as a red solid.

Preparation of TA nanoparticle. To prepare afterglow nanoparticles (TA NPs), a solution of PSMA, F127, PFODBT, and TA in tetrahydrofuran (THF) with specific concentrations was prepared. The TA NPs were synthesized using a one-step nanoprecipitation method. In this process, a solution containing TA (1 mg/mL, 0.05 mL), PFODBT (1 mg/mL, 0.05 mL), PSMA (10 mg/mL, 0.25 mL), and F127 (10 mg/ml, 0.25 mL) in THF (0.40 mL) was rapidly injected into ultrapure water (6 mL). Subsequently, Na_2CO_3 solution (10 mg/mL, 1 mL) was added. The mixture was sonicated for four minutes and then evaporated at 40 °C using rotary evaporation to remove excess THF. The resulting TA NPs were purified using ultrafiltration (100,000 MWCO, 3500 × *g*, 4 min). Throughout the synthesis process, the lab light was kept off to prevent unwanted reactions. Following synthesis, the nanoparticles were stored in a brown reagent bottle covered with tinfoil in a refrigerator at ~4 °C. The concentration of TA NPs was determined by measuring the absorption at 595 nm.

Preparation of MEHPPV nanoparticles (MEHPPV NPs). To prepare MEHPPV-based afterglow nanoparticles, the same synthesis process as that for TA NPs was conducted. A mixing solution was prepared, which contained MEHPPV (1 mg/mL, 0.10 mL), PSMA (10 mg/mL, 0.25 mL), F127 (10 mg/mL, 0.25 mL), and THF (0.40 mL). The solution was rapidly injected into ultrapure water (6 mL), followed by the addition of Na_2CO_3 solution (10 mg/mL, 1 mL). After sonication and purification, the as-prepared MEHPPV nanoparticles were stored in the dark at around 4 °C.

Afterglow luminescence determination. To compare the afterglow signal of TA NPs and MEHPPV-based nanoparticles, we prepared various concentrations of TA NPs or MEHPPV nanoparticles (0, 1.25, 2.5, 5.0, 7.5, and 10 μg/mL). After light irradiation (10 mW/cm^2) for 10 s and an acquisition time of 60 s, we captured their afterglow images and recorded their signal intensity using an IVIS Spectrum imaging system (Lumina XR) without excitation.

To optimize the irradiation time for exciting the afterglow of TA NPs, we used a concentration of 20 μg/mL and exposed them to various irradiation times (0, 5, 10, and 20 s, 10 mW/cm^2). The acquisition time was fixed at 60 s. We recorded the afterglow images and signals using the IVIS Spectrum imaging system (Lumina XR) without excitation.

To optimize the acquisition time for capturing the afterglow of TA NPs, we used a concentration of 20 μg/mL and applied an irradiation time of 10 s (10 mW/cm^2). We varied the acquisition times (1, 10, 20, 40, 60, 80, and 100 s) and recorded the afterglow images and signals using the IVIS Spectrum imaging system (Lumina XR) without excitation.

To determine the lifetime of TA NPs, we exposed TA NPs (30 μg/mL) to light irradiation (10 mW/cm^2) for 10 s and immediately captured the afterglow signal every 2.5 min with an acquisition time of 60 s.

To determine the photobleaching effect of TA NPs, we subjected TA NPs (30 μg/mL) to 10 cycles of light irradiation (10 mW/cm^2) and observed the signal after 0 and 60 min.

To determine the power density of white light to activate TA NPs luminescence, we treated TA NPs (20 μg/mL) with various power density irradiation (0.06, 5, 6, 8, 10, 15, 20, and 27 mW/cm^2, respectively) for 10 s, and immediately captured the afterglow signal with an acquisition time of 60 s using the IVIS Spectrum imaging system (Lumina XR) without excitation.

Preparation of DNA1-modified TA NPs. TA nanoparticles (TA NPs) modified with amino-labeled DNA1 were prepared by conjugating an amide bond (CO–NH) between the carboxyl group of TA NPs and amino groups on DNA1 molecules. The procedure involved dispersing TA NPs solution (1 mL, 80 μg/mL) and DNA1 (100 μL, 100 μM) in 1× DPBS (pH 7.4, 2 mL) through shock treatment, followed by the addition of EDC (250 mM) and stirring for 4 h. The reaction solution was then purified three times with H_2O using ultrafiltration (100,000 MWCO, 3500 × *g*, 5 min) and stored at 4 °C.

To determine the number of DNA1 molecules conjugated to TA NPs, 20 μg/mL (50 μL) of TA NPs were mixed with various concentrations of 20 μM DNA1 (0.78, 1.56, 3.12, 6.25, and 9.38 μL, respectively) in 1× DPBS (pH 7.4, 0.2 mL) through shock treatment. EDC (250 mM) was then added, and the mixture was stirred for 4 h. The solution was purified using Microsep™ Advance Centrifugal Devices (30k, Pall Corporation) through centrifugation (3500 × *g* for 5 min) to collect free DNA1 in solution. The concentration of free DNA1 was measured using a UV-vis spectrophotometer.

Synthesis of $FeMnO_x$ nanoparticles. Manganese-doped iron oxide nanoparticles ($FeMnO_x$) were synthesized using the following procedure[37]. First, iron-erucate complexes were prepared by dissolving 10.2 g of erucic acid (30 mmol, 80%, Aladdin) and 2.7 g of iron chloride ($FeCl_3{\cdot}6H_2O$, 99%, 10 mmol) and in 50 mL of methanol. Next, a solution of 1.2 g of sodium hydroxide (30 mmol, 96%) dispersed in 100 mL of methanol was slowly added to the iron-erucate complex solution at 40 °C under magnetic stirring. After the completion of the reaction, the precipitate containing the iron-erucate complex was washed thrice with deionized water and methanol. The resulting complex was then dried in a vacuum for 12 h.

To prepare the manganese-oleate complex, 1.44 g of manganese chloride ($MnCl_2{\cdot}4H_2O$, 10 mmol, 98%) and 5.65 g of oleic acid (20 mmol, Aladdin, 96%) were dispersed in 50 mL of methanol[37]. Next, a solution of 0.8 g of sodium hydroxide dispersed in 100 mL of methanol was slowly added to the manganese-oleate complex solution at 40 °C under magnetic stirring. After the completion of the reaction, the solution was then transferred to a separating funnel, and the upper organic layer containing the manganese-oleate complex was washed several times with distilled water. The resulting complex was dried in a vacuum for 12 h.

Finally, $FeMnO_x$ nanoparticles were synthesized by the simultaneous thermal decomposition of the manganese-oleate complex and iron-erucate complex in the presence of oleyl alcohol and oleic acid in benzyl ether or 1-octadecene[37]. In a typical synthesis of 3 nm-sized $FeMnO_x$, 1.5 mmol of the manganese-oleate complex (1.0 g), 2 mmol of the iron-erucate complex (2.14 g), 2 mmol of oleic acid (0.57 g), and 6 mmol of oleyl alcohol (1.61 g) were dissolved in 10 g of benzyl ether at room temperature. The mixture was then heated to 265 °C at a speed rate of 5 °C/min and maintained for 30 min under a constant argon flow. After cooling the mixture to room temperature, 20 mL of ethanol was added and the precipitated nanoparticles were separated by centrifugation. The as-synthesized $FeMnO_x$ nanoparticles were dispersed in chloroform and stored at 4 °C. The quantitation of $FeMnO_x$ (Fe + Mn) was performed using ICP-MS.

Synthesis of FeO_x nanoparticles. In order to synthesize ultra-small iron oxide nanoparticles (FeO_x), the first step involved preparing the iron-oleate complex[42,43]. This was achieved by reacting 10.8 g of iron chloride hexahydrate ($FeCl_3{\cdot}6H_2O$, 10 mmol, 99%) with 36.6 g of sodium oleate (98%) in a mixture of 80 mL ethanol, 60 mL water, and 140 mL hexane at a temperature of 70 °C for a duration of 4 h. Subsequently, the organic phase containing the iron-oleate complex was washed three times with water. Any excess hexane was removed through rotary evaporation, resulting in the obtained dried iron-oleate complex.

To proceed further, 3.6 g of the iron-oleate complex and 6.44 g of oleyl alcohol were dissolved in 20 g of diphenyl ether. The mixture was then heated to 70 °C under vacuum for 1 h to eliminate any presence of oxygen and water. Subsequently, the temperature of the mixture was raised to 250 °C and maintained for a period of 30 min. Following the removal of the heating source, the colloid was stirred until it cooled down to room temperature. The FeO_x solution was then washed with cyclohexane and precipitated using acetone. Finally, the purified FeO_x was dispersed in chloroform and stored at a temperature of 4 °C. The quantification of FeO_x (Fe) was performed using ICP-MS.

Preparation of phosphorylated polyethylene glycol. Phosphorylated polyethylene glycol (p-PEG-N_3) was synthesized through the reaction of oxhydryl-poly (ethylene glycol)-azide (HO-PEG-N_3, M_w = 2000 Da) and phosphoryl chloride ($POCl_3$)[37]. To prepare p-PEG-N_3, 250 mg of HO-PEG-N_3 in 1.875 mL of tetrahydrofuran was added dropwise (one drop per second) to a mixture containing 125 μL of $POCl_3$ and 1.875 mL of tetrahydrofuran in an ice bath. The resulting solution was stirred for 4 h and the products were precipitated and washed with diethyl ether three times. The phosphorylated p-PEG-N_3 was then dried in vacuo at room temperature.

Preparation of $FeMnO_x$@BHQ_3-N_3. $FeMnO_x$@BHQ_3-N_3 was prepared using $FeMnO_x$, BMPA, AA, and p-PEG-N_3. In a typical experiment, 7.5 mg of $FeMnO_x$ was transferred into a mixed solution of chloroform (4 mL) and N, N-dimethylformamide (4 mL). Then, p-PEG-N_3 (5 mg), BMPA (150 mg), AA (15 mg), and NH_2-BHQ_3 (80 μg) were added. The mixture was shaken for 12 h at 30 °C. After the reaction, $FeMnO_x$@BHQ_3-N_3 was precipitated with ice ether and washed three times with water using ultrafiltration (100,000 MWCO, 3500 × *g*, 5 min). The as-prepared $FeMnO_x$@-N_3 was dispersed in water and stored at 4 °C.

Preparation of FeO_x@BHQ_3-N_3. FeO_x@BHQ_3-N_3 was prepared similarly by mixing FeO_x (5 mg), BMPA (150 mg), AA (15 mg), NH_2-BHQ_3 (80 μg), and p-PEG-N_3 (5 mg) in a mixed solution of chloroform and N, N-dimethylformamide (1:1, v:v, 8 mL). After shaking for 12 h at 30 °C, FeO_x@BHQ_3-N_3 was collected by precipitating with ice ether and washing with water. The as-prepared FeO_x@-N_3 was dispersed in water and stored at 4 °C.

Preparation of DNA2 modifying $FeMnO_x$. The conjugation of alkyne-DNA_2 and $FeMnO_x$@BHQ_3-N_3 was carried out using a previously reported protocol (*3*). In a typical procedure, alkyne-DNA2 (10 nmol) was mixed with $FeMnO_x$@-N_3 solution (containing 1 mg Fe + Mn). A small volume of the $CuSO_4$, ascorbic acid (AA), and THPTA mixture was added to achieve final concentrations of 200 μM $CuSO_4$, 2 mM AA, and 800 μM THPTA, respectively, for the click reaction. The solution was incubated at 37 °C for 4 h and then purified with water by ultrafiltration (10,000 MWCO, 3500 × *g*, 5 min). The resulting $FeMnO_x$-DNA2 was dispersed in water and stored at 4 °C.

MRI determination of $FeMnO_x$. To test the MRI performance of $FeMnO_x$, a series of certain concentrations of $FeMnO_x$@BHQ_3-N_3 solution (Mn + Fe, 0, 0.027, 0.053, 0.11, 0.21, and 0.31 mM, respectively) were prepared for MRI determination.

MRI determination of FeO_x. To test the MRI performance of monodispersed FeO_x, a series of certain concentrations of FeO_x@BHQ_3-N_3 solution (Fe, 0, 0.028, 0.056, 0.11, 0.22, and 0.43 mM, respectively) were prepared for MRI determination.

MRI images and relaxation time were collected following acquisition parameters of the 7T-MRI animal system:

FOV = 40 × 40 mm^2,

Matrix = 256 × 256,

Slice thickness = 0.7 mm;
T_1 MRI:TR = 280 ms, TE = 4.5 ms,
T_2 MRI: TR = 2800 ms, TE = 35 ms,

Assembly of TA NPs-DNA1 and $FeMnO_x$-DNA2. APE1 responsive probe (APE1-probe) was prepared by mixing TA NPs-DNA1 (100 μL, 50 μg/mL) and $FeMnO_x$-DNA2 (62.5 μL, 1 mg/mL) in 1× DPBS containing 50 mM NaCl and 5 mM $MgCl_2$ at 37 °C for 6 h. Then, samples were purified with DPBS by ultrafiltration (10,000 MWCO, 3500 × *g*, 5 min). The obtained TA NPs-$FeMnO_x$ assembly (APE1-probe) was redispersed in 1× DPBS.

Determination of assembly ratio between TA NP-DNA1 and $FeMnO_x$-DNA2. To optimize the assembly ratio of TA NPs-DNA1 and $FeMnO_x$-DNA2 for the TA NP-$FeMnO_x$ assembly (APE1-probe), we mixed 30.3 μL of TA NPs-DNA1 (at a concentration of 33 μg/mL) with various volumes of $FeMnO_x$-DNA2 (ranging from 0 to 64 μL, with concentrations of 0.78 mg/mL) in the presence of 50 mM NaCl and 2.5 mM $MgCl_2$. After a 4-h incubation, the afterglow signal was collected using an IVIS Spectrum imaging system (Lumina XR) with no excitation, an irradiation time of 10 s, white light irradaition of 10 mW/cm^2, and an acquisition time of 60 s.

Core-satellite probe for afterglow and MRI imaging of APE1 activity with larger dynamic range and higher sensitivity

APE1-activated afterglow of APE1-probe. APE1-probe (containing 5 μg/mL TA NPs) was incubated with various concentrations of APE1 enzyme (0, 0.2, 0.5,1, 2, 4, 6, 8, and 10 U/mL, respectively) in 1× Nebuffer (10 mM Bis-tris propane-HCl, 10 mM $MgCl_2$, 100 μg/ml BSA, pH = 7.0) with final volume of 100 μL. After incubation at 37 °C for 2 h, afterglow imaging of the solution was recorded using an IVIS Spectrum imaging system (Lumina XR) (no excitation, white light irradiation of 10 mW/cm^2, irradiation time of 10 s, and acquisition time of 60 s).

APE1-activated MRI of APE1-probe. The relaxation time of APE1-probe (containing 5 μg/mL TA NPs) incubated with various concentrations of APE1 enzyme was measured using a Bruker Minispec analyzer (60 MHz). The T_1 or T_2 MRI images and T_1 or T_2 relaxation time were collected using a 7T-MRI animal system.

To acquire the mapping images of APE1-probe treated with APE1 or not, APE1-probe (containing 5 μg/mL TA NPs) was incubated with APE1 (10 U/mL) in 1× Nebuffer. After 4 h, the above solution was diluted into various concentrations (Fe + Mn, mM) for mapping imaging. in contrast, various concentrations of APE1-probe untreated with APE1 were determined as the control groups.

To conduct selectivity experiments of APE1-probe, we incubated APE1-probe (5 μg/mL) with various types of enzymes including DNase I (5 U/mL), BSA (500 ng/mL), MMP-2 (500 ng/mL), and APE1 (4 U/mL) respectively, then arranged them for afterglow imaging using the IVIS Spectrum imaging system (Lumina XR) with a white light irradiation (10 mW/cm^2), irradation time of 10 s, and an acquisition time of 60 s. Besides, T_1 and T_2 MRI were collected using a 7T-MRI animal system.

Assembly of TA NPs-DNA1 and $FeMnO_x$-DNA2. APE1 responsive probe (APE1-probe) was prepared by mixing TA NPs-DNA1 (100 μL, 50 μg/mL) and $FeMnO_x$-DNA2 (62.5 μL, 1 mg/mL) in 1× DPBS containing 5 mM $MgCl_2$ and 50 mM NaCl at 37 °C for 6 h. Then, samples were purified with DPBS by ultrafiltration (10,000 MWCO, 3500 × *g*, 5 min). The obtained TA NPs-$FeMnO_x$ assembly (APE1-probe) was redispersed in 1× DPBS.

Preparation of DNA2 modifying FeO_x. FeO_x-DNA2 was prepared by mixing FeO_x@BHQ_3-N_3 (containing 1 mg Fe), alkyne-DNA2 (10 nmol), $CuSO_4$, THPTA, and AA for the click reaction. As-prepared FeO_x-DNA2 were dispersed in H_2O and stored at 4 °C conditions.

Assembly of TA NPs-DNA1 and FeO_x-DNA2. TA NP-FeO_x assembly was prepared by mixing TA NPs-DNA1 (100 μL, 50 μg/mL) and FeO_x-DNA2 (62.5 μL, 1 μg/μL) in 1× DPBS containing 2.5 mM $MgCl_2$ and 50 mM NaCl at 37 °C for 6 h. Then, samples were purified with DPBS by ultrafiltration (10,000 MWCO, 3500 × *g*, 5 min). The obtained TA NPs-FeO_x assembly was redispersed in 1× DPBS.

MRI determination of APE1-activated TA NP-FeO_x. To test the response of TA NP-FeO_x assembly, TA NP-FeO_x (containing 5 μg/mL TA NPs) probe was incubated with various concentrations of APE1 enzyme (0, 0.1, 0.5,1, 2, 3, and 4 U/mL, respectively) in 1× Nebuffer (10 mM Bis Tris Propane-HCl, 10 mM $MgCl_2$, 100 μg/ml BSA, pH = 7.0) with final volume of 100 μL. After incubation at 37 °C for 2 h, the T_1 or T_2 MRI images were collected using a 7T-MRI animal system.

MRI images and relaxation time were collected following acquisition parameters of the 7T-MRI animal system:
FOV = 40 × 40 mm^2,
Matrix = 256 × 256,
Slice thickness = 0.7 mm;
T_1 MRI:TR = 280 ms, TE = 4.5 ms,
T_2 MRI: TR = 2800 ms, TE = 35 ms,
T_1 mapping images: TR = 356–5500 ms, TE = 8.5 ms;
T_2 mapping images: TR = 2200 ms, TE = 8–96 ms;

APE1-activated afterglow/MRI imaging for monitoring radiation dose-dependent APE1 expression in cancer cells

Preparation of DNA-3 modified TA NPs. TA NPs-DNA3 was prepared by mixing a solution of TA NPs (1 mL, 80 μg/mL) with DNA1 (100 μL, 100 μM) dispersed in 1× DPBS (pH = 7.4, 2 mL). The mixture was then treated with EDC (250 mM) and stirred for 4 h. The reaction solution was purified with H_2O by ultrafiltration (100,000 MWCO, 3500 × *g*, 5 min) three times for purification and stored at 4 °C.

Preparation of APE1-ir-probe. The APE1 irresponsive probe (APE1-ir-probe) was prepared by mixing TA NPs-DNA3 (100 μL, 50 μg/μL) with $FeMnO_x$-DNA2 (62.5 μL, 1 mg/mL) in the presence of 5 mM $MgCl_2$ and 50 mM NaCl at 37 °C for 6 h. Subsequently, the samples were purified with DPBS by ultrafiltration (10,000 MWCO, 3500 × *g*, 5 min). The obtained APE1-ir-probe was redispersed in 1× DPBS.

Afterglow imaging and MRI performance determination of APE1-ir-probe. To test the MRI performance of APE1-ir-probe, APE1-ir-probe (containing 5 μg/mL TA NPs) was incubated with 4 U/mL APE1 or without APE1 in 1× Nebuffer solution (100 μL final volume). After incubation at 37 °C for 2 h, afterglow images and MRI images of the solution were recorded.

Cell culture. HeLa cells (human cervical cancer cells) were cultured in DMEM supplemented with 1% antibiotics penicillin/streptomycin (100 U/mL) and 10% fetal bovine serum in a humidified incubator at 37 °C with 5% CO_2.

APE1-activated afterglow/MRI imaging for cancer cells. To detect APE1-activated afterglow and MRI in living cells, HeLa cells were seeded into a 6-well plate for 24 h and then treated with APE1-ir-probe (containing 10 μg/mL TA NPs) and APE1-probe (containing 10 μg TA NPs) for 4 h. In addition, HeLa cells were incubated with the APE1 inhibitor CRT0044876 (300 μM, 1 mL DMEM) for 2 h, and then the inhibitor-treated cells were incubated with APE1-probe (containing 10 μg/mL TA NPs, 1 mL DMEM) for 4 h. The treated cells were then collected after DPBS washing and counted for afterglow imaging and MRI.

To detect radiation-mediated afterglow and MRI of cells, HeLa cells were seeded into a 6-well plate for 24 h, and then the cells were treated with various doses of radiation (0, 2, 4, and 6 Gray). After 2 h, the treated cells were incubated with APE1-probe (containing 10 μg/mL

TA NPs) for 4 h. The cells were collected after DPBS washing, counted, and diluted to specific concentrations (0, 0.5, 0.75, 1.0, 1.5, and 2.0×10^7 cells/mL, respectively) for afterglow imaging, or specific concentrations (0, 0.4, 0.8, 1.2, 1.6, and 2.0×10^7 cells/mL, respectively) for MRI imaging.

Detection of protein expression at cellular level. To assess intracellular protein expression using western blot assay, HeLa cells were plated in 12-well plates for 24 h and subjected to varying radiation doses ranging from 0 to 6 Gray. After 2 h, the cells were gently washed twice with cold 1 × DPBS to remove any residual contaminations. Next, the cells were lysed using 50 μL of ice-cold RIPA Lysis for 30 min for extracting intracellular protein. The protein concentration was then accurately measured using a Microvolume UV–Vis spectrophotometer. A specific amount of extracted protein was mixed with 5× SDS-PAGE protein loading buffer from Beyotime Biotechnology (Shanghai, China). The mixture was incubated at 95 °C for 10 min to ensure complete denaturation of the protein. Following denaturation, the total proteins were separated by SDS-PAGE and transferred onto polyvinylidene difluoride (PVDF membranes, FFP32, Beyotime). The membranes were blocked with 5% BSA for 1 h at room temperature, incubated with primary antibody Tubulin (AF1216, 1:1000, Beyotime) overnight at 4 °C, alternately washed using the TBS (ST661, Beyotime) and TBST (99.9%TBS/0.1% Tween 20, v/v) buffer for three time, incubated with HRP-conjugated secondary antibodies (A0208, 1:1000, Beyotime) for 60 min, and imaged with enhanced chemiluminescence detection system. Subsequently, the membranes were rinsed in distilled water for 5 min, rinsed using protein elution buffer (P0025, Beyotime) on a shaker for 5 min, rinsed in distilled water for 5 min. As-eluted membranes were incubated with primary antibody APE1 (ab137708, 1:1000, Abcam) overnight at 4 °C, alternately washed using the TBS and TBST buffer for three times, incubated with HRP-conjugated secondary antibodies for 60 min, and imaged with enhanced chemiluminescence detection system. The quantification of specific protein bands were analyzed using Image J software.

Afterglow/MRI Imaging for monitoring radiation dose-dependent APE1 in tumor in vivo

Animal experiment. for establishing the subcutaneous xenograft tumor model, a suspension of HeLa cells (50 μL, 5×10^6 cells, in DPBS) was subcutaneously implanted. Once the tumor size reached ~6–8 mm, the mice underwent in vivo MRI imaging.

Preparation of DNA4-modified $FeMnO_x$. To prepare $FeMnO_x$-DNA4, alkyne-DNA4 (10 nmol) was mixed with $FeMnO_x$@-N_3 solution (containing 1 mg Fe + Mn). Then, a small volume of the mixture of $CuSO_4$, ascorbic acid (AA), and THPTA was added to achieve final concentrations of 200 mM $CuSO_4$, 2 mM AA, and 800 mM THPTA, respectively, under click reaction conditions. After incubation at 37 °C for 4 h, the mixture was purified with H_2O by ultrafiltration (10,000 MWCO, 3500 × *g*, 5 min). The $FeMnO_x$-DNA4 particles were then dispersed in H_2O and stored at 4 °C.

Preparation of APE1-probe (no targeting). APE1-probe (no targeting), which does not contain the tumor-targeting aptamer AS1411, was prepared by assembling TA NPs-DNA1 and $FeMnO_x$-DNA4. Specifically, TA NPs-DNA1 (100 μL, 50 μg/mL) was mixed with $FeMnO_x$-DNA4 (62.5 μL, 1 mg/mL) in 1× DPBS containing 5 mM $MgCl_2$ and 50 mM NaCl at 37 °C for 6 h. The samples were then purified with DPBS by ultrafiltration (10,000 MWCO, 3500 × *g*, 5 min). The resulting APE1-probe (no targeting) was re-suspended in 1× DPBS.

Afterglow and fluorescence imaging for tumor in vivo. To evaluate the targeting imaging of the probe in vivo, mice bearing subcutaneous HeLa xenograft tumors were treated with various doses of radiation in situ (0 and 6 Gray, respectively). After 2 h, the mice were intravenously injected with APE1-probe (no targeting) that does not contain the tumor-targeting AS1411 aptamer (120 μL, containing 80 μg/mL TA NPs). Afterglow imaging of the mice was performed using an IVIS Spectrum imaging system (Lumina XR) with no excitation wavelength, 10 s of light irradiation (10 mW/cm^2), and 60 s of acquisition time. Fluorescence imaging was captured with an excitation wavelength of 605 nm and emission in the Cy5.5 channel.

To investigate the radiation dose-dependent afterglow imaging of APE1-probe, mice bearing subcutaneous HeLa xenograft tumors were treated with various doses of radiation in situ (0, 2, 4, and 6 Gray, respectively). After 2 h, the mice were intravenously injected with APE1-probe (120 μL, containing 80 μg/mL TA NPs) for afterglow imaging using the IVIS Spectrum imaging system with no excitation wavelength, 10 s of light irradiation (10 mW/cm^2), and 60 s of acquisition time. After intravenous injection for 8 h, tumors, and major organs of the mice from each group were harvested for ex vivo afterglow imaging (10 s of light irradiation, 10 mW/cm^2, and 60 s of acquisition time).

MRI imaging for tumor in vivo. For MRI of mice injected with APE1 probe (no targeting), mice bearing subcutaneous HeLa xenograft tumors were intravenously injected with APE1 probe (no targeting) (120 μL, containing 80 μg/mL TA NPs). The mice were then scanned using a 7T-MRI scanner (Pharma Scan 70/16 US, Burker) with T_1 and T_2 sequences.

To determine the radiation dose-dependent MRI of mice in vivo, mice bearing subcutaneous HeLa xenograft tumors were treated with various doses of radiation in situ (0, 2, 4, and 6 Gray, respectively). After 2 h, the mice were intravenously injected with APE1-probe (120 μL, containing 80 μg/mL TA NPs), and then scanned for MRI imaging. The MRI images were collected using the following acquisition parameters of the 7T-MRI animal system: FOV = 40 × 40 mm^2, Matrix = 256 × 256, Slice thickness = 0.7 mm; T_1 MRI: TR = 280 ms, TE = 4.5 ms; T_2 MRI: TR = 2800 ms, TE = 35 ms.

Longitudinal and transversal subtraction enhanced imaging (L&T-ESI) for tumor. Subtractive MRI images of the tumor and their quantification were reconstructed from datasets using Image J software. The details of the subtraction process and origin images are displayed in Supplementary Fig. 52. The T_1 MRI images and T_2 MRI images of the tumor were collected at different time points (5 min, 0.5 h, 1 h, and so on) after injecting APE1-probe. The original T_1 MRI images at 5 min were subtracted from the later T_1 MRI images at 1 h to obtain ΔT_1 MRI images. Similarly, ΔT_2 MRI images were acquired by subtracting the original T_2 MRI images at 5 min from the later T_2 MRI images at 1 h. Finally, the ΔT_1 images were transversally subtracted (T-SEI) from the ΔT_2 images to acquire ΔT_1–ΔT_2 images. Overall, ΔT_1–ΔT_2 images were obtained via longitudinal and transversal subtraction-enhanced imaging (L&T-ESI) from the T_1 MRI images and T_2 MRI images.

Afterglow/MRI imaging for early prediction of tumor radiotherapy effects

Detection of intratumor ROS generation. To detect the generation of reactive oxygen species (ROS), DNA damage, and APE1 levels in the tumor, the tumors were collected 10 h after radiation treatment ranging from 0 to 6 Gray (8 h after injection of the APE1-probe). The tumors were blocked with cryo-embedding media (OTC) and prepared for cryo-sections. For the detection of ROS generation, the tumor slices were stained with DCFH-DA (10 μM) and DAPI (1 μg/mL) for 30 min, respectively. Fluorescence (FL) images were recorded using a Confocal Laser Scanning Microscope with an excitation wavelength of 488 nm and an emission wavelength of 500–530 nm.

Detection of DNA damage. To detect the level of DNA damage, the tumor slices were stained with H_2AX antibody (AF5836, 1:500, Beyotime) for 12 h, Cy3-labeled IgG H&L secondary antibodies (A0516, 1:500 Beyotime) for 6 h, and DAPI (1 μg/mL) for 0.5 h, respectively. Fluorescence images were recorded using a Confocal Laser Scanning Microscope with an excitation wavelength of 560 nm and emission wavelength of 600–720 nm.

Detection of intratumor APE1 expression. To detect the level of APE1 expression, the tumor slices were stained with APE1 antibody (1:500) for 12 h, Cy3-labeled IgG H&L secondary antibodies (1:500) for 6 h, and DAPI (1 μg/mL) for 0.5 h, respectively. Fluorescence images were recorded using a Confocal Laser Scanning Microscope with an excitation wavelength of 560 nm and emission wavelength of 600–720 nm.

Radiotherapy for tumor in vivo. To study the therapy effect dependent on radiation dosage, mice bearing subcutaneous HeLa xenograft tumors were treated with various doses of radiation in situ (0, 2, 4, and 6 Gray, respectively). Each group contained 5 mice. The body weight and tumor volume of the mice were recorded every two days. The tumor volume was calculated using the formula: volume (mm^3) = 0.5 × width^2 × length.

Histopathological analysis of tumor tissue. For the histopathological analysis, the tumors were collected on the 12th day of therapy monitoring. The tumors were embedded in paraffin, sectioned, and stained with H&E and Tunnel staining. The H&E images were recorded using a digital slice scanning system (Pannoramic MIDI) and analyzed with Case Viewer software. Tunnel images were collected using Microscopy detection with Cy3, which emits red fluorescence (excitation wavelength of 510–560 nm and emission wavelength of 590 nm).

Afterglow/MRI for evaluating radiation-induced liver organ injury

APE1-probe for afterglow/MRI imaging of radiation-treated liver organ in mice. Mice without xenograft tumors were subjected to various doses of radiation in the liver region (0, 2, 4, and 6 Gray, respectively). After 2 h, the mice were intravenously injected with APE1-probe (120 μL, containing 80 μg/mL TA NPs). Afterward, afterglow and MRI images were recorded at different time intervals. The afterglow images were acquired using the IVIS Spectrum imaging system with no excitation wavelength, white light irradiation (10 mW/cm^2) of 10 s, and acquisition time of 60 s. parameters on a 7T-MRI animal system: The MRI images were acquired using the following parameters on a 7T-MRI animal system: Field of View (FOV) = 40 × 40 mm^2, Matrix = 256 × 256, Slice thickness = 0.7 mm, T_1 MRI: TR = 280 ms, TE = 4.5 ms, T_2 MRI: TR = 2800 ms, TE = 35 ms.

Detection of intratissue ROS generation in the liver organ. To detect ROS generation, DNA damage, and APE1 levels within the radiation-treated liver, the liver region of mice was exposed to various doses of X-ray radiation (0, 2, 4, and 6 Gray, respectively). After 8 h, the liver organs were harvested and cryo-embedded. Cryo-sections were prepared for further analysis. For ROS detection, the liver tissue slices were stained with DCFH-DA (10 μM) and DAPI (1 μg/mL) for 30 min. Fluorescence images were recorded using a Confocal Laser Scanning Microscope with an excitation wavelength of 488 nm and an emission wavelength range of 500–530 nm.

Detection of intratissue DNA damage in liver organ. To assess DNA damage levels, the liver tissue slices were stained with H_2AX antibody (1:500) for 12 h, Cy3-labeled IgG H&L secondary antibodies (1:500) for 6 h, and DAPI (1 μg/mL) for 0.5 h. Fluorescence images were captured using a Confocal Laser Scanning Microscope with a Cy3 fluorescence excitation wavelength of 560 nm and an emission wavelength range of 600–720 nm.

Detection of intratissue APE1 expression in liver organ. To determine the expression levels of APE1, the liver tissue slices were stained with APE1 antibody (1:500) for 12 h, Cy3-labeled IgG H&L secondary antibodies (1:500) for 6 h, and DAPI (1 μg/mL) for 30 min. Fluorescence images were captured using a Confocal Laser Scanning Microscope with a Cy3 fluorescence excitation wavelength of 560 nm and an emission wavelength range of 600–720 nm.

Histopathological analysis of liver organ tissue. For histopathological analysis, the liver organ tissues were embedded in paraffin and sectioned for hematoxylin and eosin (H&E) staining. The H&E images were recorded using a digital slice scanning system (Pannoramic MIDI) and analyzed with Case Viewer software.

Hematology analysis. After anesthesia, we irradiated mice (n = 5 mice per group) without xenograft tumors at varying doses (0, 2, 4, and 6 Gray) directed specifically to the liver region, using a lead shield to protect the head and abdomen of mice. Those mice were sacrificed at 24 h post irradiation and the blood samples were collected for blood biochemistry assay by Wuhan Service bio Technology, which included key liver function tests.

Afterglow/MRI imaging for observing the radiation-induced abscopal effect

To establish a subcutaneous xenograft dual-sided tumor model, 1×10^7 HeLa cells were inoculated on two sides of nude mice. The mice were then divided into two groups: Group 1 and Group 2. Group 1 consisted of mice with subcutaneous dual-sided HeLa xenograft tumors, of which the right tumor was treated with 6 Gray of radiation while the left tumor was shielded with a lead plate. After 2 h, the mice received an intravenous injection of APE1-probe (150 μL, containing 80 μg/mL of TA NPs). Subsequently, afterward, afterglow, and MRI images were recorded at different time intervals. Afterglow imaging of the mice was performed using an IVIS Spectrum imaging system (Lumina XR) with no excitation wavelength, 10 s of light irradiation (10 mW/cm^2), and 60 s of acquisition time. The mice were scanned for MRI imaging. In contrast, Group 2 mice with dual-side tumors were directly intravenously injected with APE1-probe (150 μL, containing 80 μg/mL of TA NPs) for MRI imaging. This group served as the control group.

MRI images were obtained using the following acquisition parameters on a 7T-MRI animal system: Field of View (FOV) = 40 × 40 mm^2, Matrix = 256 × 256, Slice thickness = 0.7 mm, T_1 MRI: TR = 280 ms, TE = 4.5 ms, T_2 MRI: TR = 2800 ms, TE = 35 ms.

To determine the expression levels of APE1, we selectively irradiated the right tumor with 6 Gray (right tumor of Group 1, +X-ray) while shielding the left tumor from X-ray irradiation (left tumor of Group 1, −X-ray). 8 h after radiation, the tumor tissue slices from Group 1 were stained with APE1 antibody (1:500) for 12 h, Cy3-labeled IgG H&L secondary antibodies (1:500) for 6 h, and DAPI (1 μg/mL) for 30 min. As a control, the tumor slice from the nude mice with right and left tumors received no X-ray radiation was used for a comparison.

Reporting summary

Further information on research design is available in the Nature Portfolio Reporting Summary linked to this article.

Data availability

All data of this study are available in the main text and its supplementary files. Any additional requests for information can be directed to, and will be fulfilled by, the corresponding authors. Source data are provided with this paper.

References

1. Citrin, D. E. Recent developments in radiotherapy. *N. Engl. J. Med.* **377**, 1065–1075 (2017).
2. Jiang, W. et al. Hierarchical multiplexing nanodroplets for imaging-guided cancer radiotherapy via DNA damage enhancement and concomitant DNA repair prevention. *ACS Nano* **12**, 5684–5698 (2018).
3. Price, J. M., Prabhakaran, A. & West, C. M. L. Predicting tumour radiosensitivity to deliver precision radiotherapy. *Nat. Rev. Clin. Oncol.* **20**, 83–98 (2023).
4. Ehlerding, E. B., Grodzinski, P., Cai, W. & Liu, C. H. Big potential from small agents: nanoparticles for imaging-based companion diagnostics. *ACS Nano* **12**, 2106–2121 (2018).
5. Fridlyand, J. et al. Considerations for the successful co-development of targeted cancer therapies and companion diagnostics. *Nat. Rev. Drug. Discov.* **12**, 743–755 (2013).
6. Jørgensen, J. T. The current landscape of the FDA approved companion diagnostics. *Transl. Oncol.* **14**, 101063 (2021).
7. St Pierre, T. G. et al. Noninvasive measurement and imaging of liver iron concentrations using proton magnetic resonance. *Blood* **105**, 855–861 (2005).
8. Wang, L. V. & Yao, J. A practical guide to photoacoustic tomography in the life sciences. *Nat. Methods* **13**, 627–638 (2016).
9. Lucero, M. Y. & Chan, J. Photoacoustic imaging of elevated glutathione in models of lung cancer for companion diagnostic applications. *Nat. Chem.* **13**, 1248–1256 (2021).
10. Wu, L. et al. H_2S-activatable near-infrared afterglow luminescent probes for sensitive molecular imaging in vivo. *Nat. Commun.* **11**, 446 (2020).
11. Wischhusen, J. et al. Ultrasound molecular imaging as a non-invasive companion diagnostic for netrin-1 interference therapy in breast cancer. *Theranostics* **8**, 5126–5142 (2018).
12. Nguyen, N. T., Pacelli, A., Nader, M. & Kossatz, S. DNA repair enzyme poly(ADP-Ribose) polymerase 1/2 (PARP1/2)-targeted nuclear imaging and radiotherapy. *Cancers* **14**, 1129 (2022).
13. Bodei, L. et al. Molecular profiling of neuroendocrine tumours to predict response and toxicity to peptide receptor radionuclide therapy. *Lancet Oncol.* **21**, e431–e443 (2020).
14. Rodriguez-Pastrana, I., Birli, E. & Coutts, A. S. p53-dependent DNA repair during the DNA damage response requires actin nucleation by JMY. *Cell. Death. Differ.* **30**, 1636–1647 (2023).
15. Forman, H. J. & Zhang, H. Targeting oxidative stress in disease: promise and limitations of antioxidant therapy. *Nat. Rev. Drug. Discov.* **20**, 689–709 (2021).
16. Pan, Y. et al. Simulation guided intramolecular orthogonal reporters for dissecting cellular oxidative stress and response. *Nano Today* **46**, 101573 (2022).
17. Whitaker, A. M., Flynn, T. S. & Freudenthal, B. D. Molecular snapshots of APE1 proofreading mismatches and removing DNA damage. *Nat. Commun.* **9**, 399 (2018).
18. Sak, S. C., Harnden, P., Johnston, C. F., Paul, A. B. & Kiltie, A. E. APE1 and XRCC1 protein expression levels predict cancer-specific survival following radical radiotherapy in bladder cancer. *Clin. Cancer. Res.* **11**, 6205–6211 (2005).
19. Liao, S. et al. Emerging biomedical imaging-based companion diagnostics for precision medicine. *iScience* **26**, 107277 (2023).
20. He, S., Cheng, P. & Pu, K. Activatable near-infrared probes for the detection of specific populations of tumour-infiltrating leukocytes in vivo and in urine. *Nat. Biomed. Eng.* **7**, 281–297 (2023).
21. Chai, X., Yi, D., Sheng, C., Zhao, J. & Li, L. A remotely controlled nanosystem for spatiotemporally specific gene regulation and combinational tumor therapy. *Angew. Chem. Int. Ed. Engl.* **62**, e202217702 (2023).
22. Shao, Y., Zhao, J., Yuan, J., Zhao, Y. & Li, L. Organelle-specific photoactivation of DNA nanosensors for precise profiling of subcellular enzymatic activity. *Angew. Chem. Int. Ed. Engl.* **60**, 8923–8931 (2021).
23. Yu, F., Shao, Y., Chai, X., Zhao, Y. & Li, L. Spatially selective monitoring of subcellular enzyme dynamics in response to mitochondria-targeted photodynamic therapy. *Angew. Chem. Int. Ed. Engl.* **61**, e202203238 (2022).
24. Chen, M. et al. Long-term monitoring of intravital biological processes using fluorescent protein-assisted NIR-II imaging. *Nat. Commun.* **13**, 6643 (2022).
25. Zhang, Q. et al. A telomerase-assisted strategy for regeneration of DNA nanomachines in living cells. *Angew. Chem. Int. Ed. Engl* **62**, e202213884 (2023).
26. Yue, R. et al. GSH/APE1 cascade-activated nanoplatform form for imaging therapy resistance dynamics and enzyme-mediated adaptive ferroptosis. *ACS Nano* **17**, 13792–13810 (2023).
27. Xu, C. et al. Activatable sonoafterglow nanoprobes for T-cell imaging. *Adv. Mater.* **35**, e2211651 (2023).
28. Yang, L. et al. A highly bright near-infrared afterglow luminophore for activatable ultrasensitive in vivo imaging. *Angew. Chem. Int. Ed. Engl.* **63**, e202313117 (2024).
29. He, S., Xie, C., Jiang, Y. & Pu, K. An organic afterglow protheranostic nanoassembly. *Adv. Mater.* **31**, e1902672 (2019).
30. Jiang, Y. & Pu, K. Molecular probes for autofluorescence-free optical imaging. *Chem. Rev.* **121**, 13086–13131 (2021).
31. Chen, W. et al. Near-infrared afterglow luminescence of chlorin nanoparticles for ultrasensitive in vivo imaging. *J. Am. Chem. Soc.* **144**, 6719–6726 (2022).
32. Miao, Q. et al. Molecular afterglow imaging with bright, biodegradable polymer nanoparticles. *Nat. Biotechnol.* **35**, 1102–1110 (2017).
33. Li, Y. et al. A bioinspired nanoprobe with multilevel responsive T_1-weighted MR signal-amplification illuminates ultrasmall metastases. *Adv. Mater.* **32**, e1906799 (2020).
34. Barandov, A. et al. Sensing intracellular calcium ions using a manganese-based MRI contrast agent. *Nat. Commun.* **10**, 897 (2019).
35. Yi, Z. et al. In vivo tumor visualization through MRI off-on switching of $NaGdF_4$ -$CaCO_3$ nanoconjugates. *Adv. Mater.* **31**, e1901851 (2019).
36. Yuan, Y. et al. Furin-mediated intracellular self-assembly of olsalazine nanoparticles for enhanced magnetic resonance imaging and tumour therapy. *Nat. Mater.* **18**, 1376–1383 (2019).
37. Zhang, H. et al. Ultrasmall ferrite nanoparticles synthesized via dynamic simultaneous thermal decomposition for high-performance and multifunctional T_1 magnetic resonance imaging contrast agent. *ACS Nano* **11**, 3614–3631 (2017).
38. Gong, M. et al. Targeting T_1 and T_2 dual modality enhanced magnetic resonance imaging of tumor vascular endothelial cells based on peptides-conjugated manganese ferrite nanomicelles. *Int. J. Nanomed.* **11**, 4051–4063 (2016).
39. Guo, J. et al. Large aromatic hydrocarbon radical cation with global aromaticity and state-associated magnetic activity. *Chem. Mater.* **32**, 5927–5936 (2020).
40. Kim, D. H. et al. Arterial subtraction images of gadoxetate-enhanced MRI improve diagnosis of early-stage hepatocellular carcinoma. *J. Hepatol.* **71**, 534–542 (2019).
41. Bonetto, N. et al. Spinal subtraction MRI for diagnosis of epidural leakage in SIH. *Neurol.* **77**, 1873–1876 (2011).
42. Yue, R. et al. Dual key co-activated nanoplatform for switchable MRI monitoring accurate ferroptosis-based synergistic therapy. *Chem* **8**, 1956–1981 (2022).
43. Lu, J. et al. Highly sensitive diagnosis of small hepatocellular carcinoma using pH-responsive iron oxide nanocluster assemblies. *J. Am. Chem. Soc.* **140**, 10071–10074 (2018).
44. Huang, R. X. & Zhou, P. K. DNA damage response signaling pathways and targets for radiotherapy sensitization in cancer. *Signal. Transduct. Target. Ther.* **5**, 60 (2020).

45. Chang-Claude, J. et al. Association between polymorphisms in the DNA repair genes, XRCC1, APE1, and XPD and acute side effects of radiotherapy in breast cancer patients. *Clin. Cancer. Res.* **11**, 4802–4809 (2005).
46. Xiang, D. B. et al. Chimeric adenoviral vector Ad5/F35-mediated APE1 siRNA enhances sensitivity of human colorectal cancer cells to radiotherapy in vitro and in vivo. *Cancer. Gene. Ther.* **15**, 625–635 (2008).
47. Liu, T. C. et al. APE1 distinguishes DNA substrates in exonucleolytic cleavage by induced space-filling. *Nat. Commun.* **12**, 601 (2021).
48. Long, K. et al. Small-molecule inhibition of APE1 induces apoptosis, pyroptosis, and necroptosis in non-small cell lung cancer. *Cell. Death. Dis.* **12**, 503 (2021).
49. Azzouz, D., Khan, M. A. & Palaniyar, N. ROS induces NETosis by oxidizing DNA and initiating DNA repair. *Cell. Death. Discov.* **7**, 113 (2021).
50. Zheng, J. et al. Logic-gated proximity aptasensing for cell-surface real-time monitoring of apoptosis. *Angew. Chem. Int. Ed. Engl.* **60**, 20858–20864 (2021).
51. Lu, H. et al. A pH-responsive T_1-T_2 dual-modal MRI contrast agent for cancer imaging. *Nat. Commun.* **13**, 7948 (2022).
52. Cao, R. et al. Dual-ratiometric magnetic resonance tunable nanoprobe with acidic-microenvironment-responsive property to enhance the visualization of early tumor pathological changes. *Nano Res.* **16**, 10034–10046 (2023).
53. Wang, Z. et al. Two-way magnetic resonance tuning and enhanced subtraction imaging for non-invasive and quantitative biological imaging. *Nat. Nanotechnol.* **15**, 482–490 (2020).
54. Pe'er, D. et al. Tumor heterogeneity. *Cancer Cell* **39**, 1015–1017 (2021).
55. Advancing cancer therapy. *Nat. Cancer* **2**, 245–246 (2021).
56. Dagogo-Jack, I. & Shaw, A. T. Tumour heterogeneity and resistance to cancer therapies. *Nat. Rev. Clin. Oncol.* **15**, 81–94 (2018).
57. Hausser, J. & Alon, U. Tumour heterogeneity and the evolutionary trade-offs of cancer. *Nat. Rev. Cancer* **20**, 247–257 (2020).
58. De Ruysscher, D. et al. Radiotherapy toxicity. *Nat. Rev. Dis. Prim.* **5**, 13 (2019).
59. Sgouros, G., Bodei, L., McDevitt, M. R. & Nedrow, J. R. Radiopharmaceutical therapy in cancer: clinical advances and challenges. *Nat. Rev. Drug. Discov.* **19**, 589–608 (2020).
60. Zhou, J. et al. APE1 promotes radiation resistance against radiation-induced pyroptosis by inhibiting the STING pathway in lung adenocarcinoma. *Transl. Oncol.* **36**, 101749 (2023).
61. Gu, X. et al. Human apurinic/apyrimidinic endonuclease siRNA inhibits the angiogenesis induced by X-ray irradiation in lung cancer cells. *Int. J. Med. Sci.* **10**, 870–882 (2013).
62. Zhu, W., Zhang, X., Yu, M., Lin, B. & Yu, C. Radiation-induced liver injury and hepatocyte senescence. *Cell. Death. Discov.* **7**, 244 (2021).
63. Wang, K. & Tepper, J. E. Radiation therapy-associated toxicity: Etiology, management, and prevention. *CA Cancer. J. Clin.* **71**, 437–454 (2021).
64. Zhang, W. et al. Real-time, volumetric imaging of radiation dose delivery deep into the liver during cancer treatment. *Nat. Biotechnol.* **41**, 1160–1167 (2023).
65. Peveler, W. J. et al. A rapid and robust diagnostic for liver fibrosis using a multichannel polymer sensor array. *Adv. Mater.* **30**, e1800634 (2018).
66. Robinson, M. W., Harmon, C. & O'Farrelly, C. Liver immunology and its role in inflammation and homeostasis. *Cell. Mol. Immunol.* **13**, 267–276 (2016).
67. Andrade, R. J. et al. Drug-induced liver injury. *Nat. Rev. Dis. Prim.* **5**, 58 (2019).
68. Kim, J. & Jung, Y. Radiation-induced liver disease: current understanding and future perspectives. *Exp. Mol. Med.* **49**, e359 (2017).
69. Huang, J. et al. A renally clearable activatable polymeric nanoprobe for early detection of hepatic ischemia-reperfusion injury. *Adv. Mater.* **34**, e2201357 (2022).
70. Zhou, Z., Yang, L., Gao, J. & Chen, X. Structure-relaxivity relationships of magnetic nanoparticles for magnetic resonance imaging. *Adv. Mater.* **31**, e1804567 (2019).
71. Mothersill, C. & Seymour, C. B. Radiation-induced bystander effects–implications for cancer. *Nat. Rev. Cancer* **4**, 158–164 (2004).
72. Prise, K. M. & O'Sullivan, J. M. Radiation-induced bystander signalling in cancer therapy. *Nat. Rev. Cancer* **9**, 351–360 (2009).
73. Daguenet, E. et al. Radiation-induced bystander and abscopal effects: important lessons from preclinical models. *Br. J. Cancer* **123**, 339–348 (2020).
74. Meier, S. L., Satpathy, A. T. & Wells, D. K. Bystander T cells in cancer immunology and therapy. *Nat. Cancer* **3**, 143–155 (2022).

Acknowledgements

This work was supported by the National Natural Science Foundation of China (grants U21A20287, G.S.; 22234003), the National Key R&D Program of China (2019YFA0210100, X.-B.Z), Shenzhen Science and Technology Program (JCYJ20210324140205013, G.S.). National Research Foundation of Korea (NRF) grant funded by the Korean government and Korea University (NoRS-2023-00208427, H.K.). The authors express their gratitude to Professor Zebing Zeng at Hunan University for providing the TA molecule and for their assistance in synthesizing these molecules.

Author contributions

Z.L. synthesized the TA molecules. R.Y.Y. synthesized all nanoparticles. H.L. and R.Y. conducted all experiments in solution. R.Y.Y., H.L., and Y.L. built all of the animal models and conducted all of the animal experiments. G.S. conceived the idea for this project. R.Y.Y. and G.S. designed the research. R.Y.Y. and Z.L. collected the raw data in all experiments. R.Y.Y., Y.W., B.Y., and G.S. analyzed all of the data and interpreted the results. R.Y.Y. and G.S. wrote the paper. G.S., X.-B.Z., H.K., and H.Q. developed the discussion. G.S. supervised all experiments. All authors provided critical feedback on the research and the paper.

Competing interests

The authors declare no competing interests.

Additional information

Supplementary information The online version contains supplementary material available at https://doi.org/10.1038/s41467-024-50688-0.

Correspondence and requests for materials should be addressed to Guosheng Song.

Peer review information *Nature Communications* thanks Lele Li, and the other, anonymous, reviewer(s) for their contribution to the peer review of this work. A peer review file is available.